Precision Transition Isotope Shift and Hyperfine Structure Measurements in Low-Lying States of Lead

by
Carter R. Anderson

Professor P.K. Majumder, Advisor

A thesis submitted in partial fulfillment
of the requirements for the
Degree of Bachelor of Arts with Honors
in Physics

WILLIAMS COLLEGE
Williamstown, Massachusetts
May 25, 2025

Abstract

This thesis details the construction, validation, and preliminary results of an experimental apparatus designed to conduct precise measurements of the transition isotope shift and, where applicable, hyperfine structure measurements in several low-lying electronic transitions of stable lead isotopes (^{204}Pb, ^{206}Pb, ^{207}Pb, and ^{208}Pb). These precision measurements serve as critical tests for theoretical models of atomic structure in complex multi-valence atoms and offer insights into fundamental nuclear properties. This work builds upon the established expertise of the Majumder lab in precision atomic measurements. To overcome Doppler broadening, a significant challenge when heating the lead sample to temperatures between 700 and 850°C, we employ a two-step Doppler-free spectroscopy scheme developed by the Majumder Lab. The apparatus utilizes two lasers: a 939 nm pump laser tuned to excite lead from the ground state (^{3}P$_0$) to the intermediate ^{3}P$_2$ state, and a 406 nm probe laser exciting the ^{3}P$_2$ to ^{3}P$_1$ state transition. The 939 nm pump laser optically pumps a narrow velocity class of atoms. It is modulated using an Acousto-Optic Modulator (AOM), which, when paired with a high-frequency lock-in amplifier, yields a Doppler-free signal. Our preliminary results for the 406 nm E1 transition isotope shift are 2437.4(4) MHz for the ^{206}Pb -^{208}Pb pair, and 4592.2(3) MHz for ^{204}Pb -^{208}Pb. For the 939 nm E2 transition, our ^{206}Pb -^{208}Pb measurement is 200.3(1) MHz and 374.8(1) MHz for ^{204}Pb -^{208}Pb. Our measurements of the 939 nm transition isotope shifts are the first direct measurements and show excellent agreement with literature values inferred from previous experiments. We also report preliminary measurements for the ^{207}Pb hyperfine constant. This thesis additionally lays the groundwork for a method for measuring ^{207}Pb transition isotope shift using a tunable fiber-based EOM, as well as making precise measurements of the transition isotope shifts for 368 and 1279 nm transitions in all stable isotopes of Pb.

Executive Summary

This thesis details the construction, validation, and preliminary results of an experimental apparatus designed for high-resolution Doppler-free spectroscopy of atomic lead. We conduct precise measurements of the transition isotope shifts (TIS) and, where applicable, hyperfine constant in several low-lying electronic transitions of lead isotopes. Such precision measurements serve as critical tests for theoretical models of atomic structure in complex multi-valence atoms and offer insights into fundamental nuclear properties. The work done by this thesis builds upon the established expertise of the Majumder lab in precision atomic measurements, extending previous studies on elements like thallium to the more challenging case of lead. Lead, with its four stable naturally occurring isotopes (^{204}Pb, ^{206}Pb, ^{207}Pb, and ^{208}Pb), presents a rich system for investigating subtle variations in atomic energy levels arising from differences in nuclear mass and charge distribution. Specifically, this thesis focuses on the 406 nm ($6s^26p^2\ ^3P_2 \rightarrow 6s^26p7s\ ^3P_1$) E1 transition and the 939 nm ($6s^26p^2$

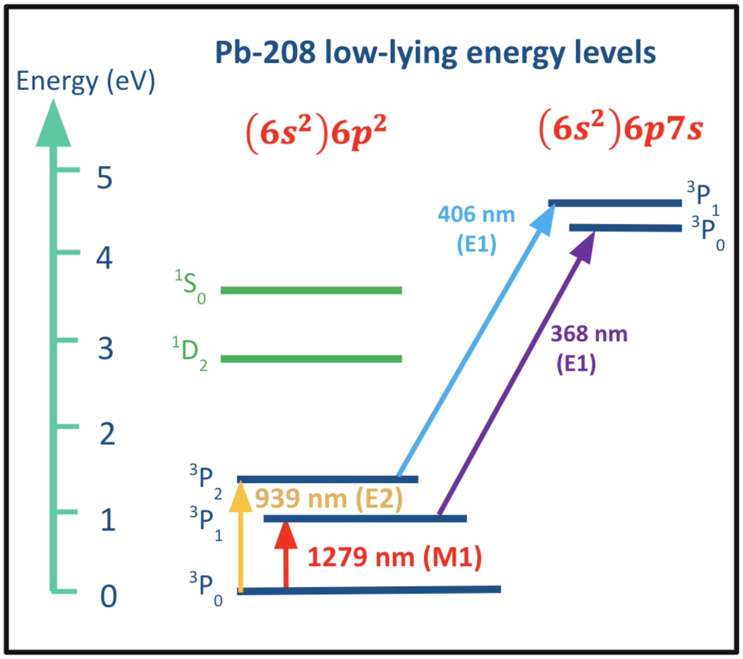

Figure 1: Selected low-lying energy levels of lead, with the relevant transitions highlighted

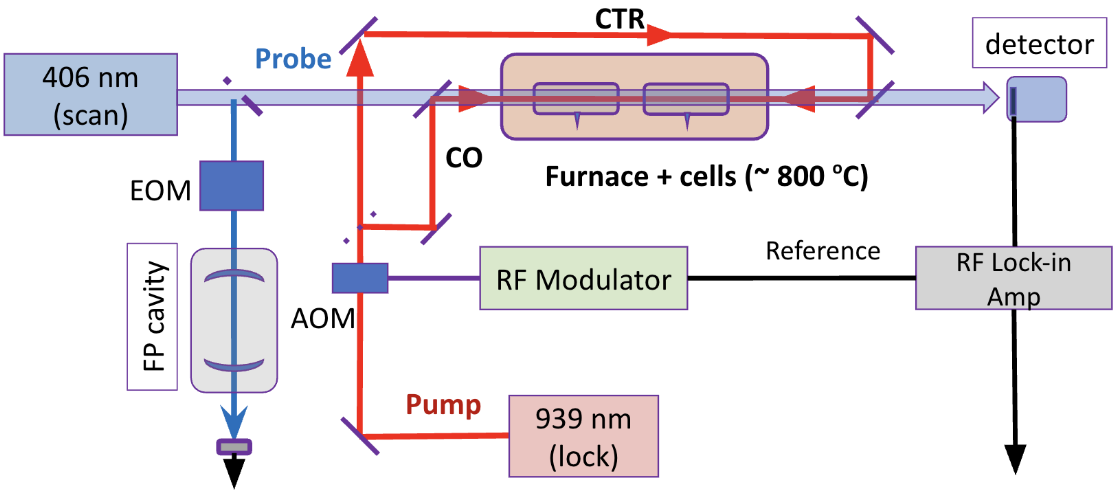

Figure 2: Schematic of the Experimental Apparatus.

$^3P_0 \rightarrow 6s^26p^2\ ^3P_2$) E2 transitions, which are shown in Figure 1. A significant challenge in performing high-resolution spectroscopy in a lead vapor cell, which requires heating the sample to temperatures between 700 and 850°C, is Doppler broadening, which can obscure the very small energy differences we seek to measure. To overcome this limitation, we employ a two-step excitation scheme coupled with a Doppler-free spectroscopy technique developed by our group. Our apparatus –shown schematically in Figure 2– utilizes two lasers: a 939 nm infrared pump laser tuned to excite lead from the ground to the $^3P_2$ state, and a 406 nm probe laser exciting the $6p^2\ ^3P_2$ to $6p\,7s\ ^3P_1$ state transition. The 939 nm laser optically pumps a narrow velocity class of atoms from the ground state to the intermediate $^3P_2$ state, selectively elevating a Doppler-free population to make the 406 nm transition and be picked out by a lock-in amplifier.

By exciting only a specific velocity group of atoms with the pump laser, we create a "hole" in the Doppler-broadened absorption profile of the ground state transition. Consequently, a population of these velocity-selected atoms are available for the subsequent 406 nm transition, leading to a Doppler-free signal. However, collisions are common within our sample at the temperature required for spectroscopy on lead, these collisions are velocity-changing, causing rapid rethermalization, scattering our velocity-selected population, broadening, and losing our Doppler-free signal.

To mitigate these effects, we employ an acousto-optic modulator (AOM) to chop our pump laser at MHz frequencies so that it is active for a shorter period of time than the characteristic time between collisions of our atoms. This rapid modulation creates a time-periodic population of the intermediate $^3P_2$ state, and subsequently a time-periodic variation in the 406 nm laser's absorption unaffected by collisions. We then use a lock-in amplifier, given the same modulation signal as reference, so it can pick out, among all the noise,

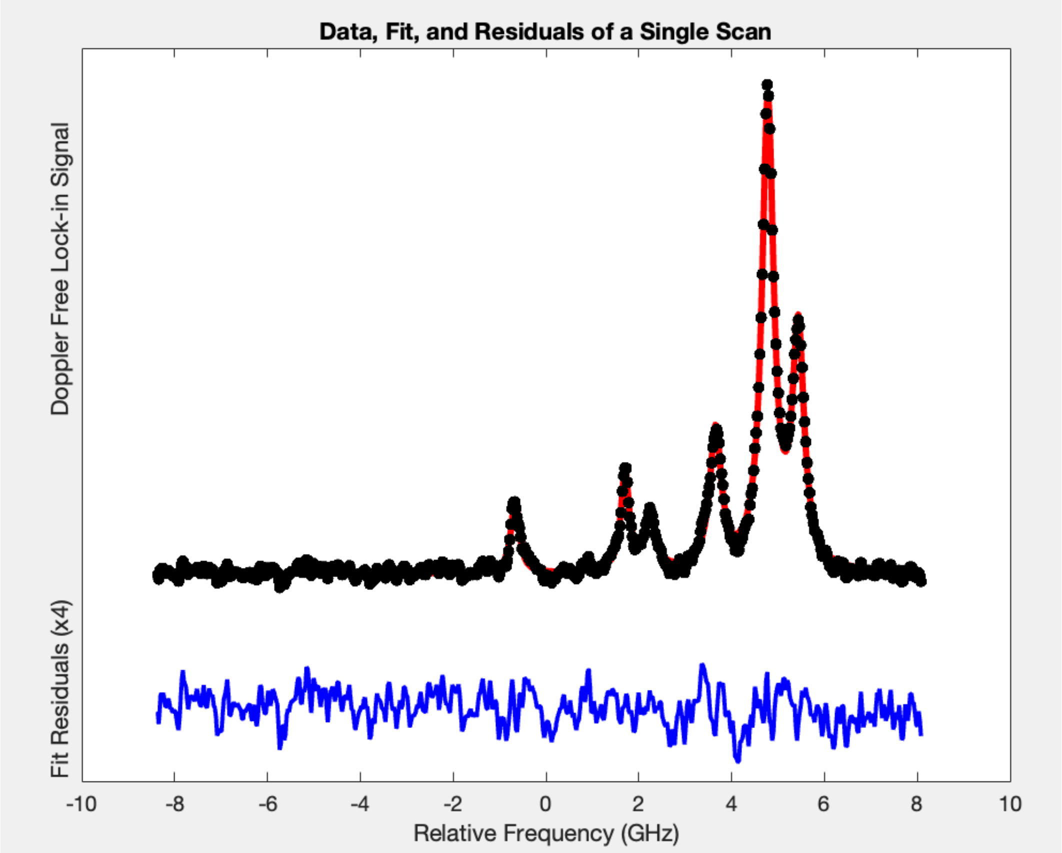

Figure 3: Top: Fitted transition isotope shift data from a Single Upscan. There are six Lorenzians: an absorption peak from both the co- and counter-propagating pump beam for each even isotope. Bottom: Magnified residuals (x4) from the experimental data fit.

only those parts of the signal with this exact modulated fingerprint. This technique allows us to selectively extract the Doppler-free Lorentzian signal from the Doppler-broadened background. A single scan, it's fit, and fit residuals are shown in Figure 3.

Our preliminary results for the 406 nm E1 transition isotope shift are 2437.4(4) MHz for the ^{206}Pb-^{208}Pb isotope pair, and 4592.2(3) MHz and for ^{204}Pb -^{208}Pb. For the 939 nm E2 transition our ^{206}Pb-^{208}Pb measurement is 200.3(1) MHz and 374.8(1) MHz for the ^{204}Pb -^{208}Pb. Our measurement of the 939 nm transition isotope shifts are the first direct measurement of this transition's isotope shift and shows excellent agreement with the literature values of 200.7(30) MHz & 375.6(40)MHz respectively. Additionally, the work presented in this thesis lays the groundwork for precise measurements of transition isotope shifts for all stable isotopes of lead in the 368 and 1279 nm transitions as well.

Acknowledgments

First and foremost, I want to express my utmost gratitude to Tiku, I started Williams Physics with you in 141 and am thankful to finish it out by working on this thesis with you. John, thank you; I would have made significantly less progress without your support every day. You made the lab a fun place, not only to ”play with laser” as my teammates say, but to hang out as well. Thank you, Graham, for reading this and for your comments. Thank you, Ben letting us not only borrow your equipment, but also for being a wonderful lab neighbor. Thank you to the Williams Swimmers & Divers I had the chance to overlap with while here. Being a part of this team has meant so much to me over the past four years. Thank you to my parents for being as supportive and encouraging of me as they always have and will be. I can't believe we thought I'd be an engineer. Physics seems far less practical and makes far more sense for me. Thank you to Tunnel City Coffee for taking my money. Molly, thank you for being there and listening the whole time. Quinn, thanks for sticking out so many psets with me (I was right every time). Oliver, I can't believe you ventured out of chem and took a physics class with me (Daniel, thank you for letting a chem kid take your class). Ruby, thank you for being the best lab partner, and John, thank you for calling our lab reports concise rather than short.

There are many more who deserve thanks, thank you.

Contents

List of Figures

Chapter 1

Introduction

1.1 Atomic Physics and Precision Measurement

Atomic physics focuses on understanding the fundamental properties and behaviors of atoms, particularly their electron configurations and interactions. Precision measurements play a crucial role in this field, allowing researchers to test and refine theoretical models of atomic structure. The Majumder lab uses precise measurements to study certain multi-valence atomic systems. This thesis, and current experiments in the lab, focus on lead, although the group has in the past also similarly studied both indium and thallium [[1],[2]]. The Majumder group at Williams also collaborates with the Safronova theoretical atomic physics group at the University of Delaware. Historically, heavy atoms with multiple valence electrons—such as thallium and lead—have played a large role in tests of fundamental symmetries, particularly in studies of atomic parity nonconservation[3]. These efforts, which gained prominence in the late 20th century, provided important experimental confirmation of the electroweak interaction and continue to motivate modern high-precision spectroscopic studies in lead .

The aim of atomic theorists, like the Safronova group, is to calculate electron wavefunctions, which describe the probability that an electron is in any given location. Such wavefunctions, as taught in quantum mechanics, can describe phenomena that have been baffling physicists for centuries. However, calculating wave functions is a difficult task; hydrogen, which only has one electron, is the only atom for which exact analytic solutions have ever been found. Elements whose atomic wave function must account for more than one electron, and their interactions, can only be modeled through the use of simplifying assumptions. The best way then to evaluate the accuracy of the wavefunction resulting from these assumptions is to validate it against a known (precise!) measurement. For certain atoms, such as the alkalis, there are both plenty of theory and experiment, but three and four-electron systems still lack much

The atoms we study are especially fascinating because of how difficult they are to model from first principles. For example, lead has 82 electrons, only four of which are valence electrons. This makes lead an incredibly difficult atom to make theoretical predictions of; our measurements then serve as a benchmark against which our atomic-theorist collaborators test their models. In the past, collaborative research between the Majumder and Safronova groups has successfully validated the theoretical understanding of lead at 1% uncertainty level. This synergy between experiment and theory continues to push the boundaries of our understanding of atomic structure [1].

1.2 Properties of lead

Lead [Pb] is a metal with atomic number 82 and a van der Waals radius of 202 pm [4]. Lead has four stable naturally occurring isotopes: ^{204}Pb, ^{206}Pb, ^{207}Pb and ^{208}Pb, with natural abundances of 1.4%, 24.1%, 22.1% and 52.4% respectively. Lead is the heaviest known stable element, and as previously mentioned, has four valence electrons with the ground state electron configuration: $[Xe]\,4f^{14}\,5s^2\,5p^6\,5d^{10}6s^2\,6p^2$ [5]. Fascinatingly, and of zero relevance to this thesis, ^{204}Pb is the only primordial (present when the Earth formed) isotope of Lead. All other isotopes, which account for a much greater proportion of the lead atoms on Earth, are radiogenic, meaning they are formed as the result of radioactive decay. Of the four stable isotopes, only ^{207}Pb possesses what is called hyperfine splitting; the very small energy differences in electronic states arising from a nonzero nuclear spin [See Section 2.1.3].

All four isotopes of lead have slightly different, or shifted, energy levels. This phenomenon is called the isotope shift. Isotope shifts arise from slight changes in the overall mass and the charge distribution of the nucleus, originating from the nuclei of different isotopes having additional (or fewer) neutrons. The transition isotope shift is further discussed in Section 2.2. This thesis aims to improve or, in some cases, make first-time measurements of transition isotope shifts, as well as measuring (when present) hyperfine splittings in several low-lying lead transitions.

Making such measurements is an excellent way to test short-range wavefunction models– the near-nucleus regime of a wavefunction– as well as nuclear structure models. In contrast, measurements of transition amplitudes or polarizability yield benchmarks for testing long-range atomic wavefunctions (further away from the nucleus). While this thesis focuses on measurements of transition isotope shifts and hyperfine splittings, the Majumder group has conducted experiments measuring long-range atomic wavefunctions as well [6].

Lead, boasting four valence and eighty-two total electrons, has an understandably complex electronic structure. Figure 1.1 depicts some of the lowest-lying energy states and the transitions from them studied in the Majumder lab. Where the excited state involves excitation of one of the two valence $6p$ electrons, we can conduct transition isotope shift measurements for all four transitions shown and will discuss them further in Chapter 3.

1.3 Laser Spectroscopy, Pumping, and Doppler-Free Spectroscopy

In the Majumder Lab, we perform laser spectroscopy. Absorption spectroscopy is the most basic form of laser spectroscopy, which utilizes the particle nature of light; since an atom can only absorb a photon whose energy exactly corresponds to an energy splitting between two given electronic states, we can investigate the energy structure of an atom by observing the way known frequencies of light interact with a sample. To observe atomic transitions, we scan lasers (in our case tunable external cavity diode lasers) over frequencies that include the atomic transitions, measuring absorption dips when the photons from the laser are of the exact same energy as an atomic transition. As previously mentioned, this experiment measures the transition isotope shift of not only the ground state 939 nm and 1279 nm transitions but also the 406 nm and 368 nm E1 transitions from $6s^26p^2$, $^3P_1$ and $^3P_2$ states to the $6s^26p7s$ $^3P_1$ and $^3P_0$ states. These transitions are from one excited state to another. Lead, a metallic element, is solid at room temperature, so laser spectroscopy requires that we heat our sample into a vapor. This is done in a quartz vapor cell heated to between 700 and 850°C in an evacuated tabletop furnace.

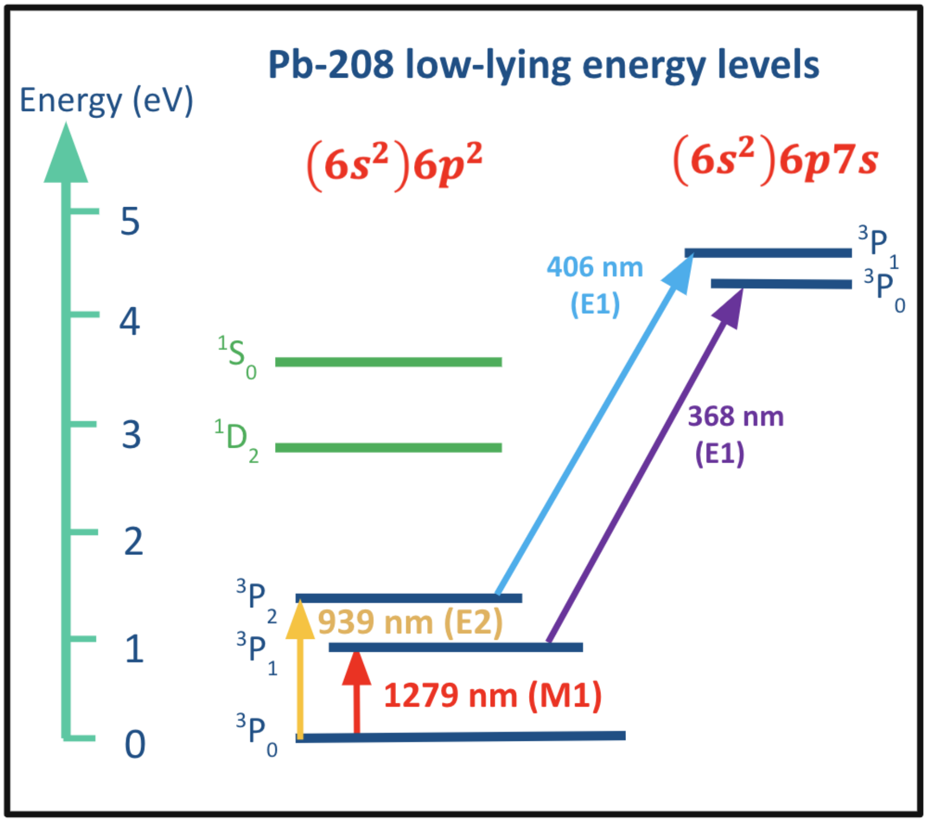

Figure 1.1: Selected low-lying energy levels of lead, with the relevant transitions highlighted

The energy level of this first excited state above the ground state, unfortunately, is large enough that in a vapor cell at 800°C, only one in a million atoms will be thermally excited to this state. A higher signal-to-noise ratio is better, so we wish to enhance this population. We can do this by optically pumping our sample, that is using another laser tuned to the energy separation between the ground and first excited state. For example, to enhance spectroscopy using the 406 nm, E1 transition, we use an infrared laser, tuned to 939 nm, to pump atoms from the ground state to the $^3P_2$ state so more atoms can interact with photons from the 406 nm laser. Heating our sample is not only required to perform laser spectroscopy but also boosts the thermal population of the $^3P_2$ state, enhancing the detectable signal, at the cost of Doppler broadening. Within the cell, especially at the temperatures present within our vapor cells, atoms travel in random directions at different speeds, each experiencing a different Doppler shift depending on how it moves relative to the incoming laser. This causes a broadening of the spectroscopic line, masking the features we wish to measure. The two-step excitation scheme developed by the Majumder Lab offers a solution to this problem; since the pump laser is tuned to a specific, known frequency, it only interacts with a specific velocity class of Doppler-shifted atoms. In doing so, only atoms of a given velocity class are pumped into an excited state, yielding a Doppler-free signal for the second transition; this technique is called hole-burning. This is not, however, a complete picture, as atoms within the vapor cell are constantly colliding with one another, and these collisions change the velocity of colliding atoms. These collisions then re-thermalize the velocity class through velocity-changing collisions. To circumvent this complication, we modulate our pump laser so the pump beam is not active long enough for re-thermalization to occur; this enables us to use a Lock-In Amplifier (The Majumder Lab's favorite instrument) for incredibly precise Doppler-free spectroscopy (See Chapter 3).

1.4 Comparison to previous work

The Majumder lab, in the past, has completed a similar study of thallium [7]. This experiment used the same two step-excitation scheme, accurately measuring both transition isotope shifts and hyperfine splittings. While conceptually similar, in practice, additional complications arise in conducting these measurements in lead. The principal complication is the vapor pressure of lead. In [7] the experiment was conducted with the sample between 400 and 500°C, due to the much higher vapor pressure of thallium. In our current experiment, we require temperatures above $700^{\circ}C$. As a result, our lead atoms move much faster than those of the previous experiment, leading to less time between collisions within the vapor cell. Where in the past a mechanical chopper wheel could modulate the pump laser, Doppler-free spectroscopy with lead requires MHz (rather than KHz) modulation; as discussed in Chapter 3, we accomplish this an instrument called an Acousto-Optic Modulator.

Previous measurements of isotope shifts and hyperfine splittings in lead exist, but are limited compared to other elements. Previous measurements include a 2000 study by Bouazza et al., measuring the 406 nm and 368 nm transition isotope shifts [8], a 2018 paper by J R Persson reporting measurements of hyperfine fine splitting [9], and a 1991 study by J. M.

Reeves and E. N. Fortson of the 1280 nm isotope shift of ^{206}Pb , ^{207}Pb relative to ^{208}Pb [10]. To date, there are *no* direct measurements of the 939 nm transition, and the 1279 nm TIS measurement has only been made for the ^{204}Pb-^{208}Pb.

1.5 Outline

The next chapter covers some relevant background material including brief discissions of: the interactions between light and atoms, atomic structure, transition isotopes shifts, broadening mechanisms, and Doppler-free spectroscopy. Chapter 3 covers the apparatus and methodology. Chapter 4 is discussion of results, and Chapter 5 is dedicated to future directions, outlining the completion of this experiment and what still need to be done. Appendix A discusses the the methodology for measuring ^{207}Pb transition isotope shifts, which requires a tuneable fiber based EOM. This is mentioned in Chapters 3 and 5 but may be best detailed separately. Appendix B contains a tabulation of all collected data.Appendix C contains fit codes used to analyze the data which can also be found in the Majumder Lab Drive.

Chapter 2

Background

Before discussing our experimental apparatus and findings, it's important to properly address the physics underlying our experiment, where the phenomena we observe originate, and what broader impact our measurements will have within the atomic physics community. In this chapter, we'll briefly discuss properties of atoms and their interactions with light, beginning with atomic structure, allowed energy states, and the isotope shifts my thesis seeks to measure. We will then discuss how light and atoms interact and ways in which it both enables and complicates our experiment.

2.1 Atomic Structure

Quantum mechanics emerged as a response to classical physics' inability to explain phenomena at microscopic scales. The concept of discrete energy levels revolutionized physics, paving the way for the quantum theory of atomic structure.

At the turn of the 20th century, Max Planck proposed energy may be quantized, and that electromagnetic radiation is emitted in discrete packets called quanta. Einstein then extended Planck's ideas to explain the photoelectric effect, demonstrating that light behaves as particles, which he called photons. Niels Bohr then introduced a model of the atom where electrons orbit the nucleus in quantized levels, with angular momentum $L = n\hbar$ where $\hbar$ is the reduced planck constant, and n is a positive integer, demonstrating these discrete energy levels. Bohr's model wholistically explained hydrogen's spectral lines but, as we now know, wasn't a complete picture and did not extend to multi-electron atoms. De Broglie proposed that particles also exhibit wave-like properties, with wavelengths $\lambda = h/\mathbf{p}$ where $\mathbf{p}$ is momentum. This led to Schrödinger's wave equation which all wavefunctions must satisfy and whose solutions describe electrons' quantized energy levels, refining Bohr's hypothesis by incorporating electron orbitals defined by quantum numbers. Throughout this chapter, we'll discuss atomic wavefunction solutions, followed by ever finer perturbations to the Hamiltonian, finding ever more complete atomic descriptions. These increasingly small perturbations yield distinct energy states we measure as tests of ongoing atomic theories.

2.1.1 Gross Atomic Structure

An atom's *gross structure* is the highest level of structure and refers to its primary energy levels derived from the principal quantum number n alone. To demonstrate this we consider the Schrödinger equation, which can be solved by the separation of variables. The radial component of the solution is given by the radial eigenstates R_{nl}. Similarly the angular components are solved by the spherical harmonics Y_{lm} where n, l, and m are all integer quantum numbers describing the discrete states, with allowable quantum numbers being integers satisfying $n > 0$, $0 \leq l \leq (n-1)$ and $-l \leq m \leq l$. The energy levels of these states (for the Hydrogen atom) are:

$$E_n = -\frac{m_e}{2\hbar^2}\left(\frac{e^2}{4\pi\epsilon_0}\right)^2 \frac{1}{n^2}, \tag{2.1}$$

where e is the elementary charge, ε_0 is the permittivity of free space, $\hbar$ is Planck's constant, and $n \in \mathbb{N}$ is the principal quantum number. It's important to notice that E_n depends only on the quantum number n. These differences in the energy levels scaling as $1/n^2$ form the foundation of atomic spectral lines. This first-order separation between states is the atomic gross structure.

With no dependence on the ℓ or m quantum numbers, there are what we call 'degenerate energies' which are multiple states with the same energy; this reflects that the gross structure does not account for additional quantum effects such as orbital angular momentum or spin interactions dependent on the other quantum numbers or relativistic corrections. These degenerate states can be separated considering perturbations to the Hamiltonian which lead to the *fine* and *hyperfine* structures covered in the following sections.

2.1.2 Fine Structure

The first deviation from the gross structure is the *fine* structure. The two mechanisms creating fine structure are relativity and electron spin-orbit coupling. Considering these effects break some of the degeneracies (those between ℓ states) in our previous energy level expression, equation 2.1, which differentiates only between states of different quantum number n. Fine structure splittings are smaller than the gross energies by a factor of roughly $1/\alpha^2$, where alpha is the fine structure constant $\approx \frac{1}{137}$.

Classically the Hamiltonian's kinetic energy term is simply $T = \mathbf{p}^2/2m_e$. However, relativistic corrections modify this to:

$$\begin{aligned} T &= \sqrt{\mathbf{p}^2c^2 + m_e^2c^4} - m_ec^2 \\ &\approx \frac{\mathbf{p}^2}{2m_e} - \frac{\mathbf{p}^4}{8m_e^3c^2}, \end{aligned} \tag{2.2}$$

where $\mathbf{p}$ is the momentum, m_e is the mass of the electron, and c the speed of light. The first term is the classical result and the second a relativistic correction; thus, the first-order correction to the Hamiltonian is,

$$H'_r = -\frac{\mathbf{p}^4}{8m_e^3c^2} \tag{2.3}$$

Each electron has a spin (an intrinsic angular momentum). This electron spin interacts with the orbital angular momentum of the electron as it orbits the nucleus. To best understand this effect, let's place ourselves in the electron's rest frame. From this perspective the nucleus, a charged object, now orbits around the electron creating a current and magnetic field. The electron then, with it's own magnetic moment arising from it's spin, experiences some shift in energy depending on the relative orientations of the magnetic vectors **B** and the electron's spin $\boldsymbol{\mu}_s$. The resulting energy shift is,

$$\Delta E = \xi(r)\,\mathbf{L}\cdot\mathbf{S} \tag{2.4}$$

where $\xi(r)$ is a radial function of how far apart the nucleus and electron are, **L** is the orbital angular momentum, and **S** the electron spin. The resulting Hamiltonian, as derived by [11], is

$$H'_{SO} = \left(\frac{e^2}{8\pi\epsilon_0}\right)\frac{1}{m_e^2c^2r^3}\mathbf{L}\cdot\mathbf{S} \tag{2.5}$$

By convention we define an operator $\mathbf{J} \equiv \mathbf{L} + \mathbf{S}$ that commutes with $\hat{H}_{SO}$. Through perturbation theory we can find the changes in energy levels. This treatment breaks degeneracies in ℓ but preserves all others.

Combining both effects, the general expression for the *fine* structure of Hydrogen is [11]:

$$E_{n,j} = -\frac{E_0}{n^2}\left\{1 + \frac{\alpha^2}{n^2}\left(\frac{n}{j+1/2} - \frac{3}{4}\right)\right\}. \tag{2.6}$$

In Hydrogen, the $2p$ state is "split" by 10^{10} Hz (10 GHz) in the microwave part of the electromagnetic spectrum. In lead the fine structure splitting of the $6p$ level is of the order 10^{14} Hz In the Infrared part of the spectrum (these are the transitions driven by our 939 and 1279 nm lasers).

2.1.3 Hyperfine Structure

In acknowledging that the nucleus has its own magnetic moment μ_I, the interaction between the magnetic moment of the nucleus and the magnetic flux $\mathbf{B}_e$ created by the orbiting electrons leads to, as no doubt you can already guess, another perturbation to the Hamiltonian called *hyperfine splitting*. The magnetic moment μ_I is dependent on the nuclear spin $\mathbf{S}_N$ by $\mu_I = g_I\,\mu_N\,\mathbf{S}_N$, where μ_N is the nuclear magneton and g_I the nuclear g-factor. The nuclear magneton is related to the Bohr magneton by the electron-proton mass ratio. The nuclear magnetic moment then is significantly smaller than that of the electron.

The Hamiltonian would be [12],

$$H'_{HFS} = -\mu_I \cdot \mathbf{B}_e \tag{2.7}$$

Following [11], the classical electrodynamic magnetic field created by a magnetic dipole μ is,

$$\mathbf{B} = \frac{\mu_0}{4\pi r^2}\left\{3(\mu \cdot \hat{r})\hat{r} - \mu\right\} + \frac{2\mu_0}{3}\mu\delta^3(r). \tag{2.8}$$

And thus the Hamiltonian,

$$H'_{HFS} = \frac{\mu_0 g_I e^2}{8\pi\, m_e m_N}\left[\frac{3(\mathbf{S}_e \cdot \hat{r})(\mathbf{S}_N \cdot \hat{r}) - (\mathbf{S}_e \cdot \mathbf{S}_N)}{r^2}\right] + \frac{\mu_0 g_I e^2}{3\, m_e m_N}(\mathbf{S}_e \cdot \mathbf{S}_N)\delta^3(r). \tag{2.9}$$

From which see can see that hyperfine splitting energy shifts depend on $<\mathbf{S}_n \mathbf{S}e>$, or the relative orientations of the electron and nuclear spins. It also follows then that hyperfine structure only exists in atoms with a non-zero nuclear spin, $\mathbf{S}_n \neq 0$, which is typically only odd isotopes – in even-numbered isotopes nucleons form up-down spin pairs resulting in a net zero spin[1]. As can be inferred by the name, hyperfine splittings are smaller than the fine structure and successfully break degeneracies preserved by the fine structure. The hyperfine splitting in Hydrogen is [11]:

$$E_{h,f} = -\frac{4 g_I \hbar^4}{3 m_N m_e^2 c^2 a_0^4} \times \begin{cases} 1/4, & \text{For triplet (spin anti-aligned).} \\ -3/4, & \text{for singlet (spin aligned).} \end{cases} \tag{2.10}$$

In the 1s state of hydrogen, this splitting is the famous "21 cm" radio-frequency line, in lead this is 1-2 orders of magnitude larger.

2.2 Isotope Shifts

In atomic physics, isotope shifts are small differences in the spectral lines of isotopes of the same element. These shifts arise primarily due to two key contributions: the mass shift and the field shift (also referred to as the volume shift). This section discusses both the mass and volume shift effects and their respective impacts on the transition isotope shifts.

The transition isotope shift in more complex (non-hydrogenic) atoms can be attributed to the effects of two factors: first differences in the [finite] nuclear mass of each isotope, and second the shift in the charge distribution. The *mass effect* is simply demonstrated by considering the kinetic energy operator in the Schrödinger equation describing multi-electron atoms [13];

$$T = \frac{\mathbf{p}_n^2}{2M} + \sum_i \frac{\mathbf{p}_i^2}{2m_e}, \tag{2.11}$$

Where $\mathbf{p}_n$ and M are the respective momentum and mass of the nucleus and $\mathbf{p}_i$ and m_e are the momentum and mass of the ith electron. Considering a stationary atom and enforcing conservation of momentum yields:

$$\mathbf{p}_n = \sum_i \mathbf{p}_i \tag{2.12}$$

---

[1] ^{207}Pb has hyperfine splitting but ^{204}Pb, ^{206}Pb, and ^{208}Pb do not.

Thus the kinetic energy operator is,

$$T = \frac{(\sum_i \mathbf{p}_i)^2}{2M} + \sum_i \frac{\mathbf{p}_i^2}{2m_e} \tag{2.13}$$

$$= \frac{\sum_i \mathbf{p}_i^2}{2M} + \frac{1}{M}\sum_{i>j} \mathbf{p}_i \cdot \mathbf{p}_j + \sum_i \frac{\mathbf{p}_i^2}{2m_e} \tag{2.14}$$

If we, for the moment, ignore the second term involving the dot product between the momenta of two electrons we are left with,

$$T = \frac{\sum_i \mathbf{p}_i^2}{2M} + \sum_i \frac{\mathbf{p}_i^2}{2m_e} \tag{2.15}$$

which can be combined using the reduced mass $Mm_e/(M + m_e)$. Ignoring the electron momenta term we can immediately see that the energy levels of an atom with a finite nuclear mass M will be raised above the stylized 'theoretical' value $E(\infty)$ of the atom whose nucleus is infinitely massive by a factor of $M/(M + m_e)$ that is,

$$E(M) = E(\infty)\frac{M}{m_e + M} \tag{2.16}$$

Utilizing $E(\infty)$ as a convenient reference we can see the difference in energy levels between two isotopes or mass M, and M' differing by δM would be:

$$\Delta E \approx \frac{m_e \delta M}{MM'} E(\infty) \tag{2.17}$$

This is the *normal mass shift.* The normal mass shift then leads to the greatest effect in the lightest atom with an effect decreasing as $1/M^2$ for increasing atomic masses, implying this shift is not significant in lead ($204 \leq M \leq 208$).

Returning to (2.13) and considering the cross-term yields another important shift in transition levels experienced known as the *specific mass shift.* This effect falls off, similar to the normal mass shift by $1/M^2$, and thus is very small in the heaviest elements. However, the specific mass shift is, in multi-electron atoms, quite difficult to calculate and unfortunately not a negligible effect,so must be considered in most atoms. Much effort has been dedicated to studying this effect in lighter elements but less so in heavier elements. This effect is demonstrated by [13] to a first approximation by treating this term of the operator as:

$$\frac{1}{M}\sum_{i>j} \mathbf{p}_i \cdot \mathbf{p}_j - (\hbar^2/M)\sum_{i>j} \nabla_i \cdot \nabla_j \tag{2.18}$$

Resulting in an energy shift away from $E(\infty)$ of:

$$\Delta E = -\frac{\hbar^2}{M}\int \psi^* \nabla_i \cdot \nabla_j \, \mathrm{d}\tau \tag{2.19}$$

where ψ is the many-electron wave function. Similar to our discussion of the normal mass shift we would then have to calculate further deviation in energies (δE) present in each isotope. While this could only be determined with incredibly precise knowledge of the wavefunction and cannot be further explored, it demonstrates the importance of both completing the wavefunction calculations (done by theoretical atomic physicists) and of taking precise measurements to inform and benchmark these challenging waveform calculations.

Although the atomic nucleus is quite small in comparison to the atom as a whole it should by no means be considered a point charge. In fact, treating the nucleus as having a finite radius r_n rather than a point varying r_n, and thus the charge distribution within the nucleus, can have a significant effect on the spectral lines. Isotope shifts arising from changes to the charge distribution or volume of the nucleus, called the *field* or *volume shift effect*, are predominant.

A first-order approximation does not entirely capture this effect, as we'd be calculating the ΔE between the electrostatic potential of a fictitious point nucleus and one with a non-zero volume (and then subsequently the δE resulting in changes to r_n) using the near nucleus electron-density, $|\psi(0)|^2$, which differs between the two regimes. Despite this complication, for pedagogical purposes here is a non-relativistic first-order approximation capable of an order-of-magnitude demonstration for heavier elements whose isotope shifts are dominated by the effect.

The contribution from each electron to the resulting shift is each electron's change in expectation value from the difference in electrostatic potential $V(r) - V_0(r)$, where $V(r)$ is the potential energy of the finite nucleus and $V_0(r)$ is that describing a point nucleus. Thus the shift in energy is,

$$\Delta E = \int_0^\infty \psi^* \left\{ V(r) - V_0(r) \right\} \psi \, 4\pi r^2 \, \mathrm{d}r \tag{2.20}$$

For $r \geq r_0$, $V(r) = V_0(r)$ Gausses law allows us to restrict the bounds of integration. Furthermore, despite potential shortcomings previously mentioned over this range, if we assume the electron charge density is approximately constant, with a value $-e\,|\psi(0)|^2$ then the energy shift is approximately:

$$\Delta E \approx |\psi(0)|^2 \int_0^{r_0} \left\{ V(r) - V_0(r) \right\} 4\pi r^2 \, \mathrm{d}r \tag{2.21}$$

For a uniform charge distribution, $V(r)$ and $V_0(r)$ respectively are

$$\begin{aligned} V_0(r) &= -\frac{1}{4\pi\epsilon_0}\frac{Ze^2}{r} && \text{and} \\ V(r) &= -\frac{1}{4\pi\epsilon_0}\frac{Ze^2}{r_0}\left(-\frac{3}{2} + \frac{1}{2}\frac{r^2}{r_0^2}\right), && \text{for } 0 \leq r \leq r_0. \end{aligned} \tag{2.22}$$

Making ΔE,

$$\Delta E = \frac{2\pi}{5}|\psi(0)|^2 \frac{Ze^2}{4\pi\epsilon_0} r_0^2 \tag{2.23}$$

The isotope shift, $\delta(E)$, then would be

$$\delta E = \frac{4\pi}{5}|\psi(0)|^2 \frac{Ze^2}{4\pi\epsilon_0} r_0^2 \frac{\delta r_0}{r_0} \tag{2.24}$$

which is conventionally re-cast as

$$\delta E = |\psi(0)|^2 \frac{\pi a_0^3}{Z} \frac{2}{5} R_\infty \left(\frac{2Zr_0}{a_0}\right)^2 \frac{\delta r_0}{r_0} \tag{2.25}$$

or both more generally, and in demonstration of where the effect originates as,

$$\delta E = |\psi(0)|^2 \frac{\pi a_0^3}{Z} C\left(Z, r_0, \frac{\delta r_0}{r_0}\right) \tag{2.26}$$

where $C\left(Z, r_0, \frac{\delta r_0}{r_0}\right)$ is a function describing the difference in charge distribution between two isotopes. Notably, discussing isotope shifts requires many assumptions and precise knowledge of waveforms [2], limiting this discussion to order of magnitude estimations. In light of this, figure 2.1 provides a comparison of the order of magnitude in electron-volts of each splitting. As shown, the Doppler width in heavier elements is much larger than isotope shifts, which presents a challenge in their measurement. The origin of Doppler broadening and the use of Doppler-free spectroscopy to counteract this effect will be discussed in subsequent sections.

2.3 Interaction Between Atoms and Light

In this work, laser spectroscopy is used to study atomic structure by sending a laser with known frequency through an atomic vapor to measure changes to the light passed through the sample. This requires an understanding of both atomic structure and the interaction of photons with atoms in the sample.

The primary atom-photon interaction of interest is the electronic transition, occurring when an electron in an atom moves from one energy level to another. These transitions can only occur when a photon's energy matches the energy gap between two atomic levels. When an electron occupies an energy state, it can absorb a resonant incoming photon, causing a transition, or jump, to the higher energy state. Intuitively, this interaction is called *absorption.* However, if an electron is already in an excited state, an incoming photon may cause it to transition to a lower energy state, emitting another photon of identical energy. This interaction is called *stimulated emission.* Absorption spectroscopy is a fundamental technique in atomic spectroscopy, which is conceptually straightforward; photons with frequencies resonant to specific atomic transitions are absorbed by atoms, whereas off-resonant photons remain unaffected. By scanning a laser over a range of frequencies and passing it through

---

[2] Predicting these volume and field shifts require both atomic theory *and* theoretical nuclear modeling, thus the uncertainties of theoretically calculated values will not be as precise as experimental values, but the presence of new experimental values can be used to test models.

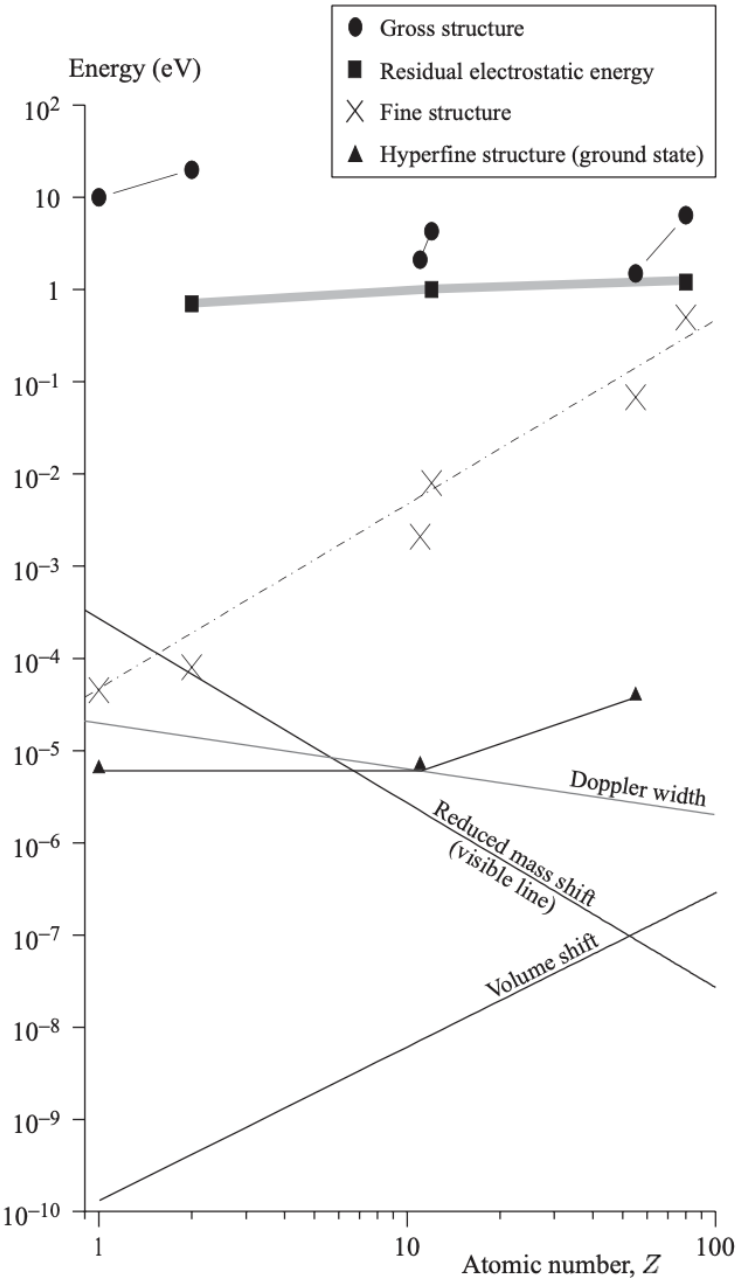

Figure 2.1: Energy of structures for various atomic number Z. Figure from [12]. Data points are Hydrogen, Helium, Sodium, Magnesium, Cesium, and Mercury, respectively. The order of magnitude of Doppler broadening indicates the importance of Doppler-free spectroscopy when measuring shifts or splitting of smaller magnitude, which would otherwise be hidden.

an atomic vapor, with a photodetector we measure the transmitted intensity. Photons being absorbed by a resonant frequency manifest as a dip in the detected signal, allowing us to measure atomic transitions. This technique is effective for strong transitions, where a significant transmission dip is observable. However, for weaker signals that are difficult to detect through basic absorption spectroscopy, more sensitive spectroscopic methods must be employed.

Another consideration in spectroscopy is the effect of laser power on electronic transitions. In low-power regimes, increasing laser power can result in a greater population of excited-state atoms. However, once the laser power reaches a certain threshold, the transition can become saturated. At saturation, the populations of the lower and upper states become equal. Since an incoming photon is equally likely to either excite a ground-state atom or stimulate emission in an excited-state atom, increasing the number of photons will not always change the relative populations of the atomic states. In this case, further increases in laser power do not significantly alter the transition dynamics. This saturation effect is crucial in precision spectroscopy, as it determines the operational limits of laser excitation and the efficiency of various spectroscopic techniques.

2.4 Broadening Mechanisms

A single atomic transition would be just that, a single transition between two exact energy levels excited by a resonant photon of that frequency. However, an actual atomic transition line is never so simple. In reality, for example, a range of frequencies, around the central "true" frequency, can drive a transition. These effects make it harder to measure the transmission dips we use to study atoms. The resulting features in the variation of intensity are the exponential: $e^{-\alpha[V(\omega,\sigma,\Gamma)]}$ where α is the optical depth, a function of the density and vapor cell length, and $V(\omega,\sigma,\Gamma)$ a convolution of a Gaussian and Lorentzian (depending on which broadening mechanisms are at play) discussed further in this section. The transitions, and then features resulting from the drop in transmitted intensity don't appear as a sharp feature as we scan in frequency across a transition. These mechanisms can be classified as either *homogeneous* broadening, where all atoms in a sample experience the same interaction, effecting their absorption frequencies equally, and *inhomogeneous* broadening when different atoms within the sample experience different local interactions, affecting the absorption frequency differently throughout the sample. In this section, we'll discuss some of the broadening mechanisms relevant to my experiment.

Homogeneous Broadening

The three most relevent sources of homogeneous broadening to this thesis are: finite lifetime (also known as natural), power, and collisional broadening. As previously mentioned, homogeneous broadening affects all atoms in a sample equally, resulting in Lorentzian lineshapes in frequency scans. Below, we discuss the mechanisms behind each type of broadening and loosely estimate their order of magnitude.

Finite Lifetime Broadening An electron will only stay in an excited state for a finite length of time [3]. Although not factually correct, I think of it akin to how electricity 'tries' to travel to the lowest potential. Electrons also 'prefer' to be in their lowest energy state, thus, it's not unreasonable to think excited states have a finite lifetime, that is, if in an excited state will spontaneously decay over time. I forgo a formal description of how the spontaneous decay occurs, as these lifetimes are well documented, and I think this personification of an electron is clear enough [and significantly less mathy]. What instead I offer is that the natural broadening of a transition is related to its quantum mechanical strength, this broadening follows the relation $\gamma(\text{MHz}) = \frac{1}{2\pi\tau}$, were τ is the upper state's lifetime. We investigate E1 and E2 transitions, and as such the full width half max (FWHM) of the natural broadening Lorentzian is on the order of 15 MHz.

Power Broadening It was previously mentioned that increasing laser power can saturate a transition; there is another complication associated with saturation called power broadening. When a transition saturates, stimulated emission shortens the lifetime of an excited state. This effect is subdued on either side of central peak, causing inhomogeneous changes across frequency and broadening the lineshape. The power-broadened line Γ_{PB} is related to the non-power broadened line by a factor of $\sqrt{1 + (I/I_{sat})}$ where I is the laser intensity and I_{sat} is the saturation intensity. Further details are discussed in [12], however I_{sat} is related to one over the lifetime, $1/\tau$, so the effect is of similar magnitude to broadening due to the finite lifetime, and thus does not significantly challenge our experiment.

Collisional Broadening A lead vapor cell contains more than a single atom and is heated to temperatures between 700 and 850°C, making collisions between atoms inevitable. These collision can, similar to finite-lifetime broadening, cause electrons to be collisionally de-excited; much like both power and natural broadening this leads to a broadening of the lineshape, only here associated with the collisions between atoms. The FWHM of this Lorentzian is:

$$FWHM = 4p\sigma\sqrt{\frac{2}{\pi\mu k_B T}}\,, \tag{2.27}$$

where p is the vapor pressure, σ the collisional cross section, μ the reduced mass of colliding atoms, k_B the Boltzmann coefficient, and T the temperature. In an evacuated Pb vapor cell at 800°C, experimentally we see this broadening is between 20 and 30 MHz, and is the dominant source of homogenous broadening we encounter in this experiment.

---

[3] However certain states like the $6s^2 6p^2\ {}^3\text{P}_1$, ${}^3\text{P}_2$ are considered "meta-stable" whose lifetimes are long enough they are considered stable and their finite lifetime broadening negligible in our experiment, clearly this follows from

Inhomogeneous Broadening

The inhomogeneous broadening mechanism relevant to our experiment is caused by the Doppler effect. Inhomogeneous broadening does not affect the atoms in a sample equally, resulting in a Gaussian broadening of the lineshape. The relevant mechanism of Doppler Broadening is discussed below.

Doppler Broadening If radiation has a frequency f in the laboratory reference frame, the frequency f' of the same radiation seen in the reference frame of a part moving at velocity $\mathbf{v}$ is $f' = \frac{\mathbf{v}}{c}f$, this is the Doppler effect. If an atom is moving with some velocity, a resonant frequency of radiation of its atomic transitions will be different than if it were stationary. In our sample, the atoms are heated to at least 700°C. Since the average speed of the atoms is related to the square-root of temperature, we experience significant broadening due to the Doppler effect.

As seen in [12], in a gas the fraction of atoms whose velocity is between v and $v + \mathrm{d}v$ is,

$$\begin{aligned} f(v)\mathrm{d}v &= \sqrt{\frac{M}{2\pi k_B T}} \exp\left[-\frac{Mv^2}{2k_B T}\right] \mathrm{d}v \\ &= \frac{1}{u\sqrt{\pi}} \exp\left[-\frac{u^2}{v^2}\right] \mathrm{d}v, \end{aligned} \tag{2.28}$$

Where $u = \sqrt{2k_B T/M}$ is the most probable speed of an atom with mass M of temperature T. If we relate this distribution of velocities to frequency we find that the absorption has a Gaussian line shape, with FWHM :

$$\mathrm{FWHM} = \frac{f_0}{c}\sqrt{\frac{8\ln(2)k_B T}{M}} \tag{2.29}$$

where f_0 is the central resonant frequency in the lab frame. At 800°C the 406 nm probe transition has a FWHM on the GHz scale, masking the transition isotope shift we seek to measure.

Voigt Convolution

Our measured spectra has contributions from both homogenous and inhomogenous broadening mechanisms and will thus be a combination of Lorentzian and Gaussian components. This lineshape can be modeled with a Voigt Convolution. Mathematically a convolution of two functions f and g is,

$$(f * g)(t) \equiv \int_{-\infty}^{\infty} f(\tau)g(t-\tau)\mathrm{d}\tau \tag{2.30}$$

which takes f and g and creates a new combined function [14]. The convolution of a Gaussian and a Lorentzian is called a Voigt Convolution. Taking such a convolution yields:

$$V\left(\omega, \sigma, \Gamma\right) = \frac{1}{\sigma\sqrt{2\pi^3}} \int_{-\infty}^{\infty} \frac{\Gamma/2}{\omega'^2 + (\Gamma/2)^2} \times \exp\left[\frac{-(\omega-\omega')^2}{2\sigma^2}\right] \mathrm{d}\omega' \tag{2.31}$$

By fitting our signal to 2.31, we can extract the location and uncertainty of an atomic transition.

2.5 Doppler-Free Spectroscopy

As described in previous sections, Doppler broadening can be a dominant factor that limits the resolution in atomic spectroscopy. This section describes Doppler-free spectroscopy through a method called saturated absorption spectroscopy. While this is *not* the method of Doppler-free spectroscopy used in this thesis, it does provide a useful introduction to the concept of Doppler-free spectroscopy as background to the description of the experimental apparatus used in this work.

Recall that atoms moving with different velocities along the direction of the laser beam experience different Doppler shifts, according to the relationship $\omega' = \omega - kv$, where ω' is the angular frequency in the atom's rest frame, ω is the laboratory frame frequency, k is the wavevector, and v is the component of the atom's velocity along the wavevector. This results in a Gaussian broadening of the spectral lines (as a form of inhomogeneous broadening) that can mask features we wish to measure. Doppler-free laser spectroscopy techniques have been developed to overcome this limitation, one such important technique is saturated absorption spectroscopy.

Consider the setup shown in Figure 2.2. In this configuration, a scanning laser beam is split into a stronger *pump beam* and a weaker *probe beam*, which travel in opposite directions through a sample cell containing the atomic vapor. The strong pump beam interacts with atoms whose velocity component along the beam axis, $v = (\omega - \omega_0)/k$, is such that the Doppler-shifted laser frequency $\omega - kv$ is resonant with the atomic transition frequency ω_0. This strong interaction saturates the transition for this specific velocity class of atoms, meaning all the atoms of the velocity class are excited to the upper level. This interaction can be described as burning a "hole" in the velocity distribution of the lower energy level population. The width of this "hole" is given by, $\Delta\omega_{hole} = \Gamma(1 + I/I_{sat})^{1/2}$, where Γ is the power-broadened homogeneous width of the transition, I is the pump beam intensity and I_{sat} is the saturation intensity. As noted in discussing the power-broadening, since I_{sat} is related to τ, $\Delta\omega_{hole}$ can be approximated as $\gamma_{\text{power}}/\Gamma_{\text{doppler}}$ which is a few percent of ω.

The weak probe beam, counter-propagating with the pump beam, also interacts with atoms with a Doppler-shifted frequency near resonance. When the laser frequency ω is far from the atomic resonance ω_0, the pump and probe beams interact with different velocity classes of atoms, and the pump beam has no significant effect on the absorption of the probe beam.

However, as the laser scan and it's frequency ω is tuned very near to the atomic resonance frequency ω_0 (i.e., $\omega \approx \omega_0$), both the pump and the probe beams interact with the

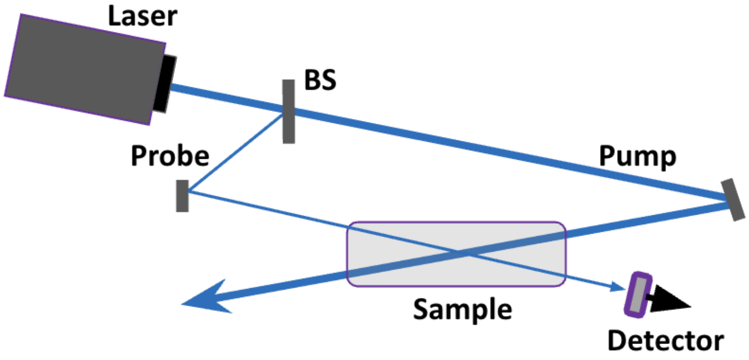

Figure 2.2: Saturated Absorption Spectroscopy Experimental Setup: A laser scans over a transition, the beam is split by a beam-splitter (BS) into a strong pump beam and a weaker probe beam. Both beams are directed through a sample, and the probe beam is analyzed in a detector.

same velocity class of atoms (those with a velocity component $v \approx 0$ along the beam axis). The significantly stronger pump beam will saturate the transition for these near-stationary atoms, leading to lower absorption of the weak probe beam; the result is a narrow peak of increased probe beam transmission. The small transmission peak from the probe beam will be superimposed on the broader Doppler-broadened absorption profile that would be observed without the pump beam. This narrow peak is Doppler-free as it originates from atoms with essentially zero velocity along the laser beam axis. This process is shown in Figure 2.3: as the laser scans and is resonant with non-stationary atoms, the probe beam is depleted with almost light being transmitted through the sample , when resonant with stationary atoms both beams will be interacting with the same atoms, the powerful pump beam will saturate the population and weaker probe beam transmit as a Doppler-free peak in the signal.

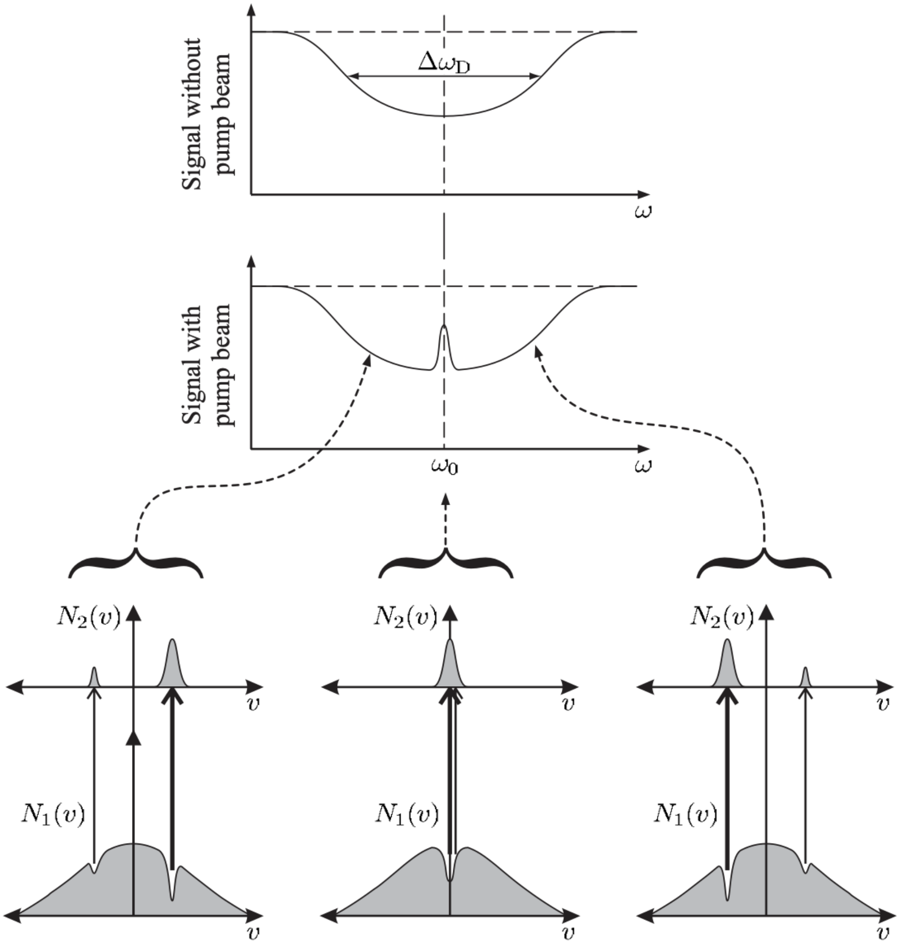

Figure 2.3: Doppler-Free Signal via Saturated Absorption Spectroscopy. As the laser frequency is scanned across an atomic transition, the probe beam absorption follows the Doppler-broadened Gaussian profile. When the laser is resonant with atoms of zero longitudinal velocity, both the pump and probe beams interact with the same velocity class, saturating the transition. This saturation reduces absorption of the probe beam, producing a narrow Doppler-free peak superimposed on the broader Doppler-broadened background. Figure from [12].

Chapter 3

Experimental Apparatus

This chapter outlines the experimental method employed in this project. The best way to understand the work is through description of the experimental apparatus. This chapter contains three sections: the first two sections provide a pedagogical introduction to the apparatus, building up our scheme conceptually, followed by a third section discussing each component in more detail.

3.1 Spectroscopy of the 406nm E1 Transition

First, if only considering spectroscopy of the 406 nm E1 transition isotope shifts[1] our experimental apparatus would follow the schematic below. The most basic method to perform spectroscopy of this transition involves scanning a laser tuned to emit light over a range (say,

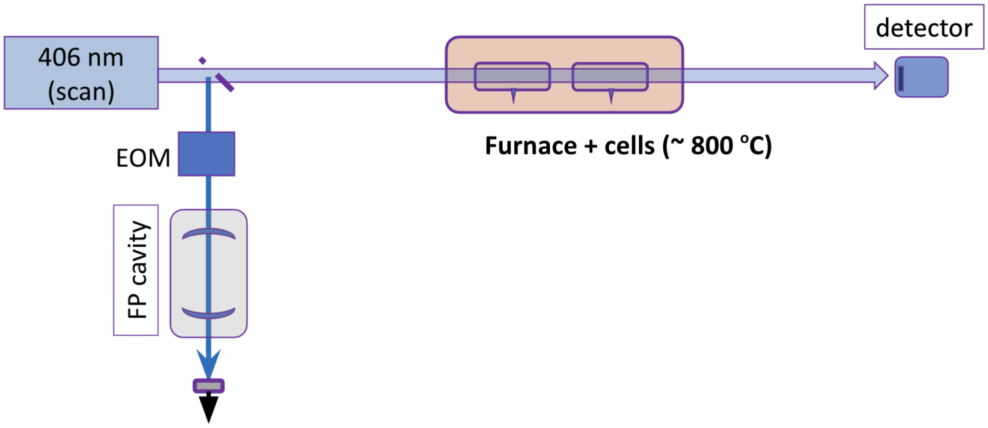

Figure 3.1: Experimental schematic of the 406nm probe laser

---

[1] From the $6s^2 6p^2\ ^3P_2$ to the $6s^2 6p7s\ ^3P_2$ state as shown in Fig 1.1.

8 GHz) centered around the 406 nm E1 transition. The beam is directed through a furnace containing the samples and into a photodetector. A small portion of the beam is also picked off by a beam splitter before the furnace, and passes through an electro-optic modulator (EOM), a Fabry-Perot cavity, and into another photo detector - this 'branch' is used as a frequency calibration to locate our signal as the laser scans.

Let's first consider what we would observe with this experimental set-up. We would, as previously mentioned, measure the transmitted intensity, the transition lineshape is given by,

$$I_t = I_0\, e^{-\alpha[V(\omega,\sigma,\Gamma)]}, \tag{3.1}$$

where I_0 is the initial intensity, α is the optical depth, and $V(\omega, \sigma, \Gamma)$ a Voigt-Convolution. The lower state, $6s^2 6p^2\ {}^3P_2$, is *not* the ground state, but in heating our samples, we thermally excite some atoms that our laser could interact with. Under the Boltzmann distribution, the fraction of atoms in an excited state N_i, compared to the ground state N_j, is

$$\frac{N_i}{N_j} = \exp\{-\Delta E_{i,j}/k_b T\} \tag{3.2}$$

Where $\Delta E_{i,j}$ is the separation in energy between the two states, T is the temperature, and k_b is Boltzmann's constant. Substituting values for the lower state of this transition, we see that, at 800°C, roughly only one in a million atoms can interact with the probe laser; we can, despite the initial population being so small, still detect absorption. The complication arises not from having such a small lower state population[2], but from Doppler broadening. Figure 3.2 shows in blue the true Doppler width at 800°C, The splitting, most importantly, is visible despite Doppler broadening at this temperature, but significantly limits precision. The absorption peaks representing the isotope shift of the 939 nm transition from the ground to intermediate state would not be resolvable using this method (for even isotopes), and would be completely masked by Doppler broadening, so fitting to a signal like this would not be possible. Thus, both cases require we develop a method of 'beating' the Doppler shift with some form of Doppler-free spectroscopy.

3.2 Optical Pumping of the 939 nm E2 Transition

By adding a second overlapping laser, a second transition can be excited before collisonal de-excitation. As mentioned, at 800°C, the thermal population of the ${}^3P_2$ state is only 10^{-6} that of the ground state. By using a laser tuned to the 939 nm transition, some of the atoms in the ground state can be optically pumped to the ${}^3P_2$ state, increasing the signal-to-noise ratio. Our pump laser, unlike that of the saturated absorption spectroscopy method presented in Section 2.5, does not scan; rather, it's locked to a fixed, known frequency. As a result, the pump beam will only excite a single velocity class of atoms. However, in a hot, dense thermal vapor, the atoms are frequently colliding, exchanging energy, and changing

---

[2] Although, as we'll touch on next, we do everything we can to increase the population of this state and our signal size.

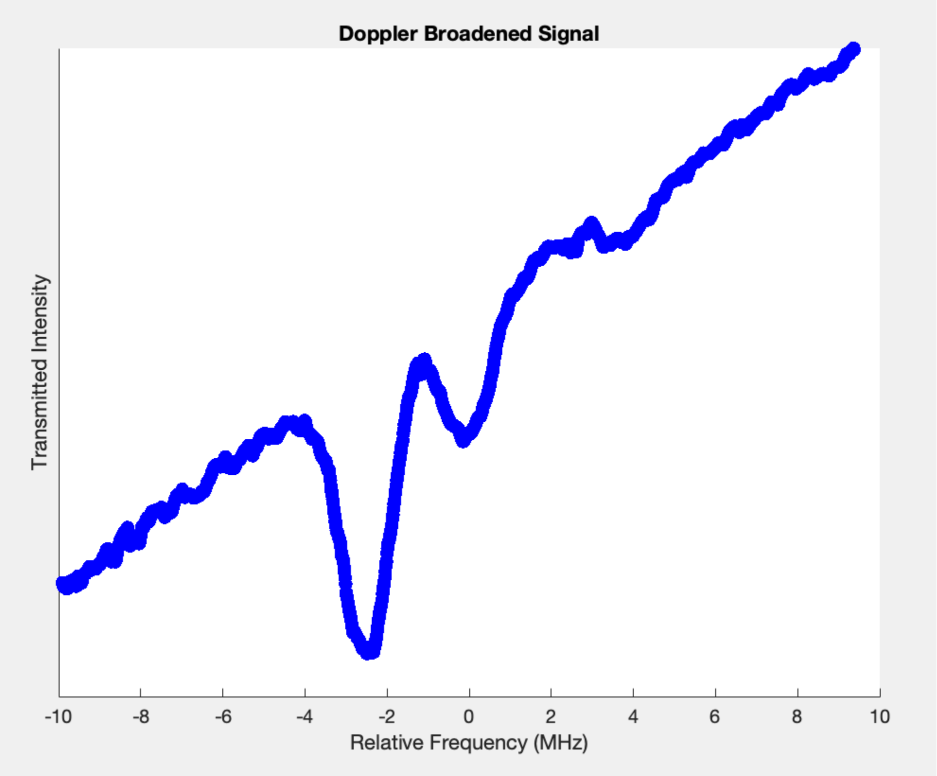

Figure 3.2: The magnitude of the Doppler broadening absorption of the 406 nm transition at 800°C, the larger two peaks are ^{208}Pb, and ^{206}Pb respectively; the smaller peak is one of the ^{207}Pb transitions. We could fit this data to the exponential $\exp\{\{-\alpha[V(\omega,\sigma,\Gamma)]\}$ where $V(\omega,\sigma,\Gamma)$ is a Voigt-Convolution, however, Doppler broadening severely limits precision, and the presence of collision could affect our measurement. The slope in the curve is the power variation in the 406 nm laser as it scans through frequency, this is modeled and easily accounted for in our fit model.

velocity. As a result, the group we pumped is quickly re-thermalized through collisions, and our Doppler-free population is lost.

Re-thermalization happens quickly, but not instantaneously, so theoretically the pump laser picks out a Doppler-free velocity class[3] for each isotope for a fraction of a second before re-thermalization occurs. Early exploration work done by Charles Yang '25 [15] demonstrated that, at 800°C, such collisions occur at a rate of $\sim$ 100kHz. Naturally, we seek a way of collecting data only when we can pick out a Doppler-free velocity class before re-thermalization occurs and the velocity class scatters. This is achieved by modulating the pump beam at a frequency such that the pump is active for a period shorter than the characteristic time between collisions of the atoms and only observing when the pump is on. The Majumder lab's favorite instrument is called a Lock-in Amplifier and does just that; it

---

[3] Atoms all moving with the same velocity, and no inhomogeneous broadening

takes in a modulated signal and a reference, demodulating the signal against the reference, outputting the difference, what is only present at the same frequency as the reference. Figure 3.3 shows a model of this effect in a two-isotope system for simplicity, notably, there is *no* fundamental difference in a three-isotope system, just an additional peak.

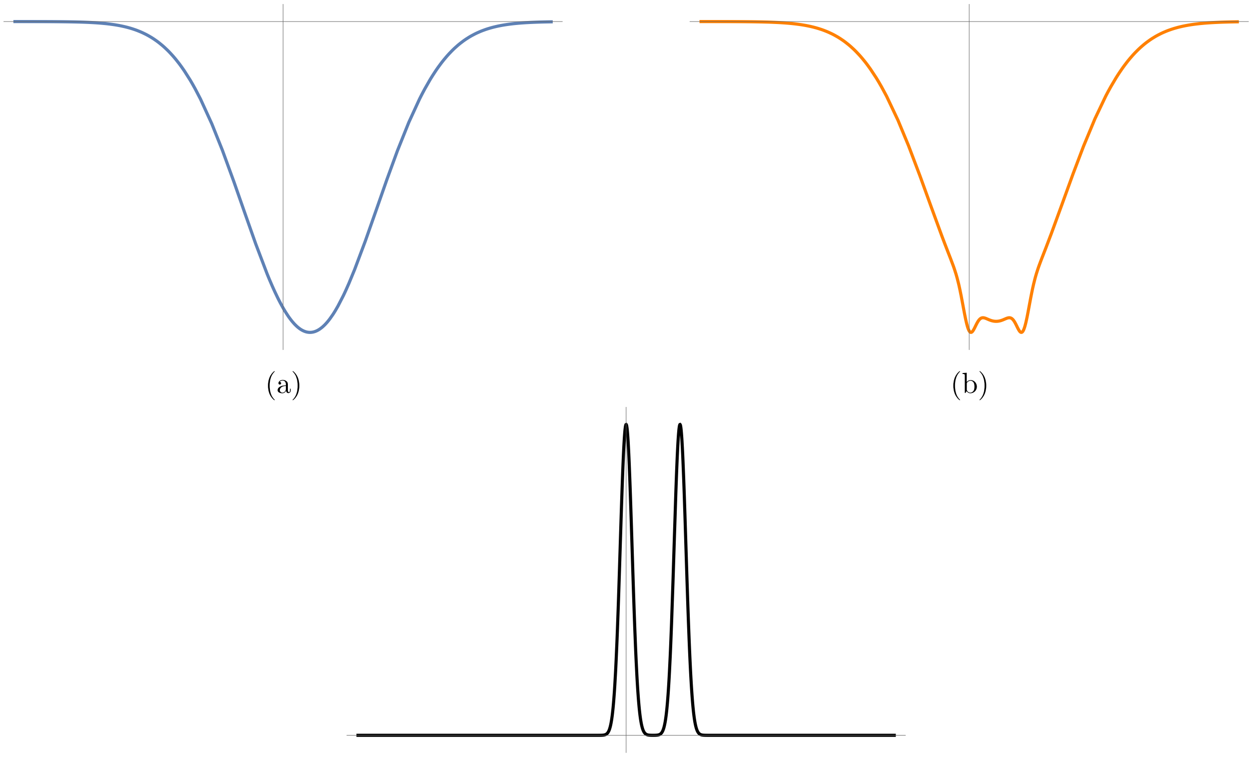

(a) (b) (c)

Figure 3.3: Comparison of signals as (a) depicts the signal without optical pumping, (b) depicts the signal with optical pumping before re-thermalization and collisional de-excitations occurs. Modulating the pump at 1 MHz -such that the period is less than the characteristic time between collisions. The signal would switch between (a) and (b) at 1 MHz. The lock-in, given the signal and a 1 MHz reference, would output (c) the 'difference', essentially only 'seeing' the small Doppler-free class picked put by pumping before re-thermalization caused by collisions can occur.

The 939 nm transition is a very weak E2 electric quadrupole transition; the effect of the optical pumping is significantly magnified in this graph for demonstration, and would not be distinguishable to the naked eye. The lock-in, however, is sensitive enough to observe this subtle effect. In fact the pump laser may only increase from thermal population of $\approx 10^{-6}$ to $\approx 10^{-5}$.

A schematic of the apparatus including the modulated optical pumping is shown in Figure 3.4. To implement the optical pump step, we have added the 939 nm *locked* laser, an

Acousto-Optic Modulator (AOM)[4], which can be used to modulate the pump laser by mixing it's steady driving signal with a function generator, a Lock-in amplifier, and the function generator that provides the modulation to the AOM and the reference for the lock-in. The electronic involved in driving the AOM are not included in this figure, for simplicity, but are discussed in Section 3.3.8.

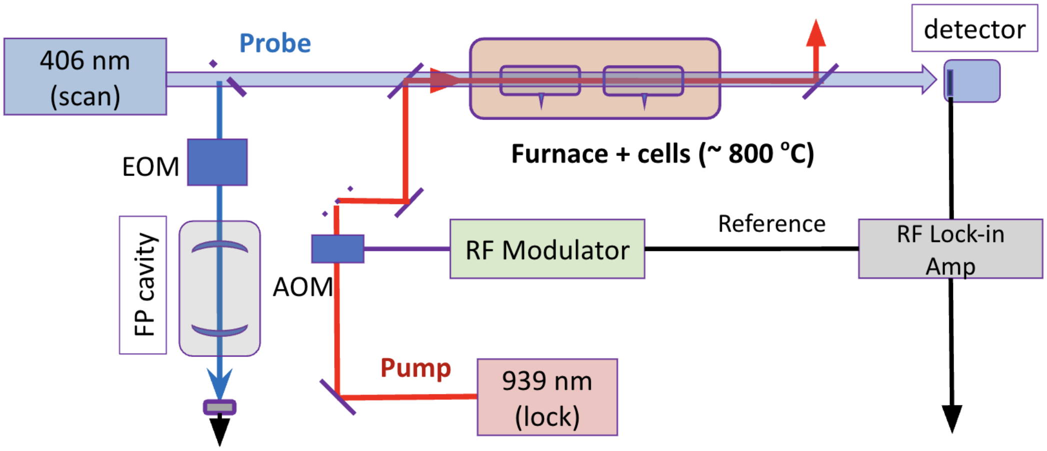

Figure 3.4: Schematic including Doppler-free Optical pumping to the $^3P_2$ state and the 406 nm probe laser.

The Doppler-shift, as given in Section 2.4, is $\Delta f = (\mathbf{v}/c)f$, where f is the frequency in the lab frame and Δf the change in frequency seen in the reference frame moving with velocity $\mathbf{v}$. The Doppler shift depends on f, and since the same transition occurs in each isotope at a slightly different frequency[5], the pump beam must be resonant with different velocity classes experiencing different Doppler shifts. The signal from each isotope is originating from a different velocity class, meaning as we see in Figure 3.5(a), the absorption peaks for each isotope are red or blue shifted away from the 'true' TIS location(depending on the exact frequency of the pump laser). We solve this by splitting our pump beam in two and running one co- (CO) and one counter-propagating (CTR) with the probe laser; this leads to 3.5(b), where each isotope has a red and blue shifted peak, from which the 'true' shift between isotopes can be extracted. Defining Δf_1 and Δf_2 to be the true transition isotope shift values for the first and second step transition of any given pair of isotopes, the apparent peak separation for the CO and CTR configurations spectra will be:

$$\Delta f_{co} = \Delta f_2 + (\omega_2/\omega_1)\Delta f_1 \tag{3.3}$$

$$\Delta f_{ctr} = \Delta f_2 - (\omega_2/\omega_1)\Delta f_1 \tag{3.4}$$

---

[4] Driven by a 110 MHz 'steady state' RF signal to produce 1st-order diffraction

[5] The Transition Isotope Shifts we're trying to measure!

Where $\Delta f_{co,ctr}$ are measured, and ω_2, ω_2 are the exactly known laser frequencies[6]. Adding both the CO and CTR we arrive at our complete apparatus shown in Figure 3.6.

3.3 Component Specifics

Given the complete schematic developed and provided in Figure 3.6, this section provides a description of each component of the apparatus.

3.3.1 406 nm Scan Laser

The 406 nm laser is an external cavity diode laser (ECDL) whose construction was begun by Charles Yang ′24 and completed by Gautam Ramasamy '26, and Karleigh Bath (Bryn Mawr College '25) in the summer of 2024. The details of its construction are outlined in Yang's thesis [15]. An external cavity diode laser is a type of laser that combines a laser diode and a diffraction grating to create a relatively inexpensive, narrow-line-width laser with an adjustable frequency output that is simple enough to be lab-built. The laser diode emits light, part of which -the zeroth-order grating reflection- exits as the laser beam, while the first-order diffracted light is reflected back into the diode, forming an external cavity between the diode and the grating. The external cavity enforces additional frequency selectivity, as only certain wavelengths are reflected back depending on the angle of the grating. The laser operates by aligning both internal and external cavity modes to create a stable single-modal laser; fine-tuning of the output involves adjusting the diode's temperature, current, and internal grating alignment.

Home-built ECDL lasers like the one we use to probe this transition are tunable and cost-effective, but not challenge-free. The primary problem, which has required many hours of tinkering, is getting the laser to lase and stably scan in a single mode; often, the laser will bounce between two different modes, providing unusable data. When scanning correctly, roughly 9 mW of power reach the vapor cell stack and 5 mW pass through all three cells.

3.3.2 939 nm Pump Laser

The pump laser tuned to the 939 nm $(6s^2)6p^2\ ^3P_0 \rightarrow\ ^3P_2$ electric quadrupole (E2) transition both increases the population of the intermediate $^3P_2$ state and provided our method for Doppler-free spectroscopy.

We use a Toptica DL Pro laser, which is an incredibly stable commercial laser when tuned to 939 nm, drifting less than a GHz overnight, and negligibly during data acquisition. It can be tuned with small adjustments to the piezo offset. The beam is modulated at MHz frequencies using the Brimrose acousto-optic modulator (AOM) discussed in section 3.2.8 We use, through an optical fiber, the Augenbraun Lab's wavemeter to monitor this laser's

---

[6] For the 939nm pump + 406nm probe laser pair this is 2.4 and 3.4 for the 1279nm pump + 368nm probe pair

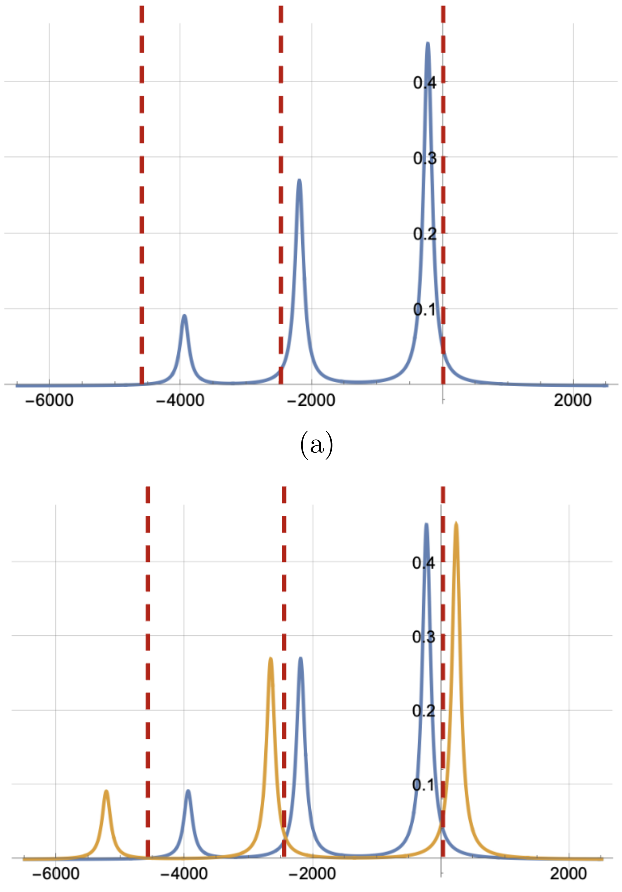

(a)

(b)

Figure 3.5: The red dashed lines are approximately where the relative positions of each isotope would be in the absence of Doppler shifts. (a) shows the signal when the pump beam co-propagates with the probe. (b) shows an example signal resulting from using both co- and counter-propagating pump beams. For display purposes, we choose here a ’lock-point’ for the IR laser between the 208 and 206 isotopic resonances.

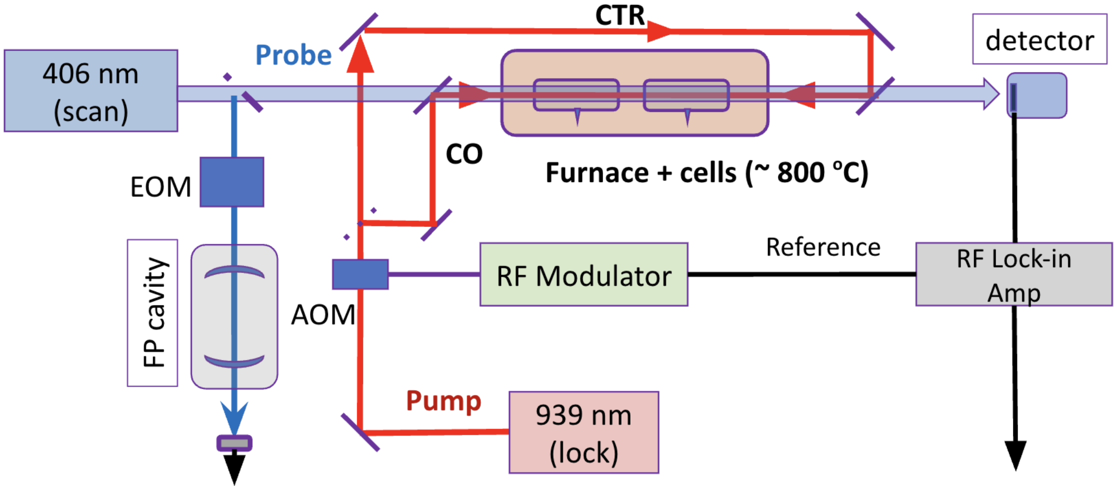

Figure 3.6: Schematic of the experimental apparatus.

frequency during our experiment. A PID loop provides feedback to the laser controller, which adjusts the piezo voltage of the frequency to keep the frequency stable at the 1 MHz level.

3.3.3 Evacuated Furnace

We use a custom-built vapor cell furnace. The furnace is driven by three variable transformers, which power three pairs of clamshell heaters that surround an evacuated ceramic tube. The furnace is frequently pumped down between scans to remove any gas and slightly backfilled with argon (to 10 mm Hg) to create an inert environment. The vapor cells themselves are situated in series within an annealed stainless steel tube within the evacuated chamber to create an even further thermally stable environment. Although absolute temperature determination is not required for our measurement, this setup provides a consistent, thermally stable environment. We monitor the temperature with three S-type thermocouples, rated to 900° C with an uncertainty of ±1° C.

3.3.4 Quartz Vapor Cells

In many of our lab's experiments, our spectroscopy is done using isotopically enriched quartz vapor cells. Recalling Chapter 1.3 the the natural isotopic abundances of lead are 52.4% ^{208}Pb, 22.1% ^{207}Pb, 24.1% ^{206}Pb, and only 1.4% ^{204}Pb. We have acquired enriched samples of each isotope from the Oak Ridge National Laboratory, using vapor cells from Precision Glassblowing, to create vapor cells of both single and pairs of isotopes. By setting up our cells in series, we can measure the isotope shift between any pair of isotopes and thus can guarantee that each TIS is measured in multiple configurations. The cells contain no buffer gases and are rated for up to 950°C. The cells are cylinders with angled face windows to avoid multiple reflections. In the case of some older cells, thermal cycling to high temperatures over time has had the effect of liberating gas from the quartz walls, leading to much higher gas density and collision rates, making our Doppler-free technique ineffective. We suspect this is due to foreign gas broadening as we don't see a systematic reduction in broadening even as the temperature (and vapor pressures) are rapidly reduced.

3.3.5 Fabry-Pérot Cavity

We use a Fabry-Pérot cavity as a frequency calibration for the 406 nm laser. A Fabry-Pérot cavity is composed of two confocal mirrors designed to transmit a portion of the incident light. As light waves traverse back and forth within the cavity, constructive interference occurs at specific resonant frequencies, leading to a buildup of intensity at these frequencies.

The resonance frequencies (ν_n) of a Fabry-Pérot cavity are given by the equation:

$$\nu_n = \frac{cn}{4L},$$

where c is the speed of light, n is an integer, and L is the length of the cavity; thus, resonant peaks are evenly spaced in frequency. The frequency separation between two adjacent resonance peaks is the free spectral range (FSR), which is $\mathrm{FSR} = \frac{c}{4L}$.

We use a Fabry-Pérot cavity with a 1 GHz free spectral range. A beamsplitter directs a small fraction of the 406 nm laser beam through the cavity into a detector to be used as a frequency reference as the laser scans. By observing the transmission peaks of the cavity as the laser frequency scans, we calibrate our scan in frequency space, like a ruler would in physical space, and linearize the scan in frequency. An example of these transmission peaks from a scanning laser is illustrated in Figure 3.7(a).

3.3.6 Electro-Optic Modulator

An electro-optic modulator (EOM) uses the electro-optic effect to control the phase, frequency, or amplitude of a laser passing through its crystal in response to an applied electric field. In our experiment, we use an EOM to phase modulate the 406 nm laser. With a 600 MHz driving frequency, the transmitted light has, in addition to the central frequency f_0, higher order side-band frequencies of $f_0 \pm 600$MHz and $f_0 \pm n * 600$ MHz for integer values of n [7]. When used, the Fabry-Pérot spectrum is the sum of several Airy Functions separated by 600 MHz.

Fitting the Fabry-Pérot with the side bands created by the EOM measures the Free Spectral range more precisely. An example of the Fabty-Pérot transmission when using the EOM is shown in 3.7(b).

---

[7] Of decreasing amplitude with increasing n

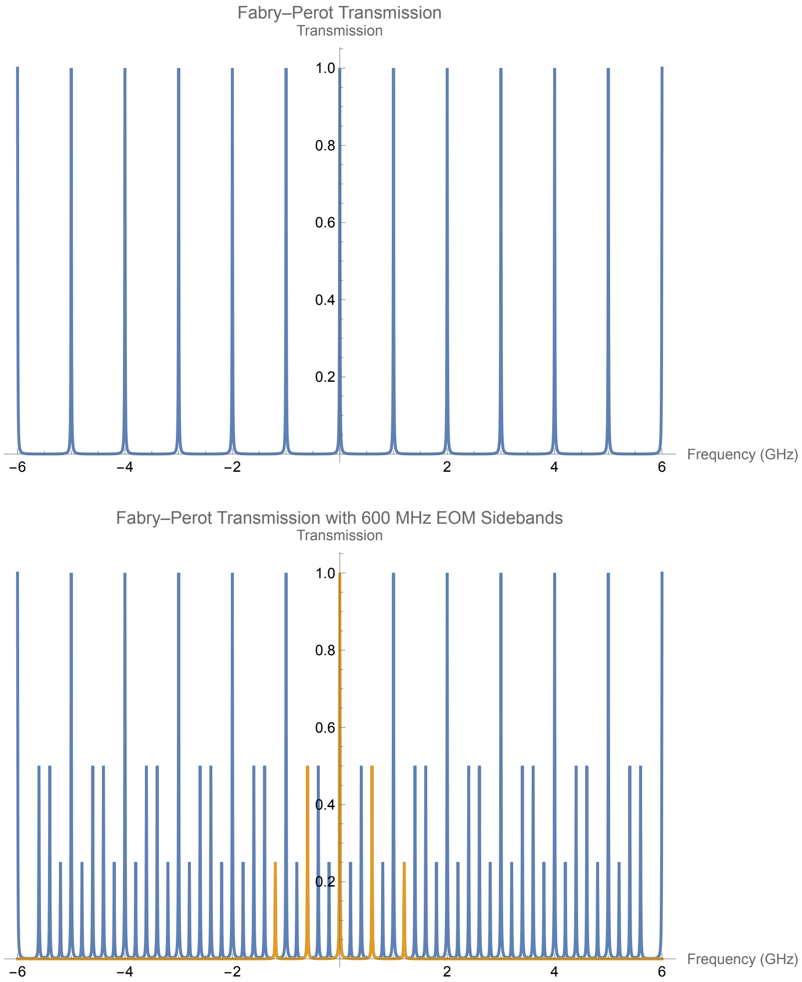

Figure 3.7: Example Fabry-Pérot transmission signal. (a) The cavity alone, FSR is 1 GHz. (b) With a 600 MHz modulation applied (via our EOM). The highlighted feature demonstrates where the zero, first, and second-order transmission peaks fall within the scan.

3.3.7 Lock-in Amplifier

A lock-in amplifier is an essential tool for extracting weak signals from noisy backgrounds by focusing on a specific modulation frequency. Fundamentally, a Lock-In picks out the portion of a signal that is present and oscillating at an input reference frequency. Effectively rejecting signal components at all other frequencies, including most of the noise. Mathematically, this process is akin to transforming the signal from the time domain to the frequency domain using a Fourier transform and then isolating the component at the modulation frequency.

The lock-in amplifier, in this thesis, is an RF lock-in amplifier[8] allowing us to demodulate MHz frequencies, where typical Lock-in amplifiers are limited to 100kHz. The 939 nm pump laser is chopped at a specific frequency using an acousto-optic modulator (AOM), leading

---

[8] Stanford Research Systems Model SR844

to a periodic variation in the population of the intermediate $^3P_2$ state, and consequently variation in the absorption spectrum of the 406 nm laser at the exact same frequency.

The lock-in amplifier multiplies the noisy input signal with a clean sinusoidal reference signal at the modulation frequency; the output is a DC signal representing the portion of the photodetector signal oscillating at the chopping frequency. In this experiment, this modulated component is the Lorentzian-Doppler-free lineshape of the atomic transitions we seek to measure. By detecting only the signal that is synchronous with the laser chopping, the lock-in amplifier effectively filters out noise and the Doppler-broadened background.

To obtain a good signal size, it is important to have the correct relative phase between the input and reference signals. This can be achieved by manually adjusting the phase until the output is optimized, or the 90° out-of-phase channel is minimized.

3.3.8 Acousto-Optic Modulator

The acousto-optic modulator (AOM) is used to modulate the 939 nm pump laser driving the E2 transition at a MHz frequency. This, as discussed in Section 3.2, is how we perform Doppler-free spectroscopy. The time-periodic variation in the 939 nm laser's intensity caused by the AOM chopping gives the modulation to the lock-in amplifier referenced to the chopping frequency.

AOMs utilize the acousto-optic effect, where acoustic excitations within a crystal interact with the light passing through it; we create a traveling wave in the crystal using a function generator, which induces strain patterns in the crystal, modulating its refractive index. The modulation works like a diffraction grating, deflecting incident light into several different orders of beams. The zeroth-order beam passes straight through, while the rest are diffracted at different angles. The frequencies of the diffracted beams are shifted by the driving frequency of the AOM (110 MHz), however we block all higher-order beams, only using the intensity-modulated zeroth-order beam.

We use a Brimrose AOM mounted on a multi-axis alignment stage, designed to transmit light at 939 nm with a driving frequency of 110 MHz. We then modulate the driving signal to create our Doppler-free signal. The electronics used to both generate the RF signal and switch it on and off are: a signal generator (Hewlett-Packard 8656B) which outputs a sinusoidal RF oscillating voltage at the AOM's driving frequency; solid state switch (Mini-Circuits ZASWA-2-50DR+) which takes the 110 MHz signal and turns it on and off based on a chopping signal from the TTL gate; TTL Gate, receives a square wave signal at the desired modulation frequency (ω_{ref}, ranging from 500 Hz to 10 MHz) from a function generator switching between zero and five volts; Amplifier (Mini-Circuits ZHL-03-5WF) which amplifies the AOM driving signal to sufficient RF power a schematic of this is shown in 3.8. Operation, testing, as well as these components and their design, are discussed extensively in [15] section 3.2.

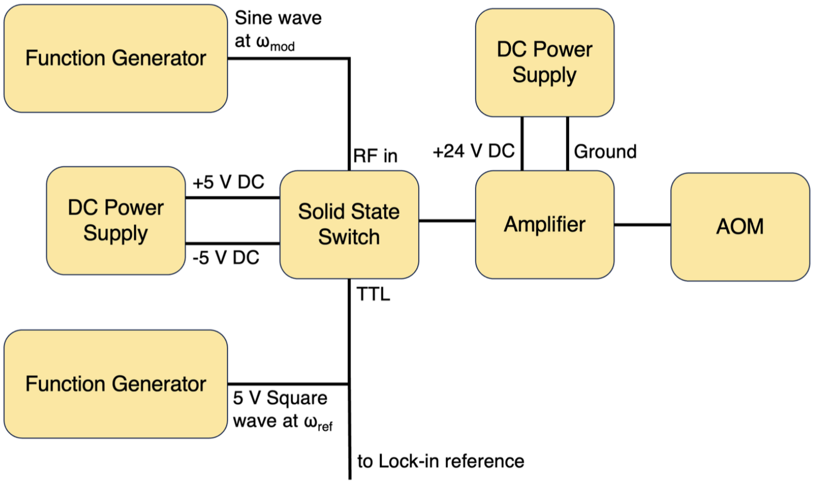

Figure 3.8: A diagram of the AOM driving electronics [15]

3.3.9 Dichroic Mirrors

A dichroic mirror is used to overlap both the Co and Counter pump beams with the probe beam before propagation through the lead vapor cells. This type of mirror exhibits wavelength-selective properties, reflecting certain wavelengths while transmitting others. In this case, the dichroic mirrors reflect the visible 406 nm laser while transmitting the 939 nm infrared light of the pump beams. Alignment is very sensitive in our experiment, these specialized mirrors allow collinear alignment of the two beams to ensure they are completely overlapped throughout the entirety of our sample.

3.3.10 Beamsplitters

Both beamsplitters are polarization-dependent prisms paired with a half-waveplate immediately beforehand. The light is split into two beams 90° apart. The percentage of power transmitted versus reflected is adjustable with the halfwave plate. Each is coated to be optimized for the wavelengths they're used for. The 406 nm laser beam splitter is set so almost the entirety of the beam is transmitted and only a small portion is picked off for the EOM and Fabry-Pérot cavity. The 939 nm beamsplitter is configured so that both the Co and Counter propagating pump beams are roughly the same strength when they reach the sample.

Chapter 4

Results & Discussion

This chapter outlines the progress and results made by this thesis. Almost the entirety of this thesis was dedicated towards constructing, testing and refining the apparatus, and making sure that we could both account for and explain everything we saw in our data. This chapter is dedicated to this process, and its sections will cover the non-exhaustive highlights of this process.

4.1 Validation

The two-step excitation scheme implemented and discussed in this thesis was not developed from scratch for the purpose of this experiment. A similar apparatus was used to measure the transition isotope shifts in ^{203}Tl and ^{205}Tl. As discussed in Section 1.4, the vapor pressure of thallium is significantly higher than lead, so this experiment required significantly lower temperatures, and getting a Doppler-free signal required far lower chopping frequencies, attainable with a simple mechanical chopper wheel. The method described for Lead in this thesis requires much higher temperatures, leading to more Doppler-broadening, requiring more complexity and new instruments. Much of the early work on this method was completed by Charles Yang [15], who investigated using an AOM to modulate optical pumping to the ^{3}P$_2$ state. Although plagued by problems with the 406 nm laser Charles was able to get a Doppler-Free signal, proclaiming in his thesis "It Actually Works!". When taking over this experiment, it was a question of getting the best signal possible, searching for any possible systematic errors, improving all sources of uncertainty, and making sure we truly understood what physics we were seeing.

Initially, the experiment was set up using a commercial furnace while our home-built, evacuated furnace was being used to complete an experiment measuring electric-dipole-transition amplitudes of ^{208}Pb excited states [6]. This time was spent making sure we could both reliably get a signal and that our 406 nm probe laser could stably scan a large enough range to encapsulate all isotope shifts. Both the transition isotope shifts and hyperfine constants measured by this thesis are frequency shifts, thus, our precision is highly affected by uncertainty in our frequency calibration. One of the first improvements made by this thesis involved exploring the free spectral range (FSR) and frequency calibration, as an incorrect FSR value used in fitting leads to a systematic shift in the data. Now, instead of periodically taking Fabry-Pérot data to verify the cavity FSR hasn't changed, the EOM is set up in a separate 'branch' where it can now be used to improve Fabry-Pérot fits during data collection.

In the fall, we were able to demonstrate that we could reliably get a signal, with a signal-to-noise ratio high enough to fit our data. The commercial furnace we were using did appear to introduce noise into our data. The furnace we were using offered the advantages of i) being easy to load, and ii) heating up very quickly [capable of reaching 800°C in 45 minutes] which was quite useful at that stage in the experiment where we needed to regularly heat up and test certain aspects of the apparatus. This tabletop furnace, however, is not evacuated, which we believe leads to unnecessary sources of noise. In January 2025, when the other experiment was completed, I completely disassembled and reconstructed the apparatus on the table housing our home-built evacuated furnace. This allowed for some optimization and reorganization of our optics. Reconstructing the experiment and re-acquiring our signal took up the entirety of Winter Study owing to recurrent troubleshooting.

The two main findings during this period, which may be relevant to a future thesis or summer student implementing a similar scheme, are discussed next. Some vapor-cells, especially those which experience many thermal cycles in the smaller furnaces, may have more Doppler broadening than others. We believe this is because when thermally-cycled many times in an environment exposed to the atmosphere, a small amount of air may eventually get into the vapor-cell; we have modeled this qualitatively and found slight differences in Doppler broadening between two cells at the same temperature at the same modulation frequency to be consistent with one of the cells having some foreign gas inside the cell. We currently have enough cells enriched with each isotope to avoid this by using fresher cells. We also found the Dichroic mirror and diffraction grating that separate the 406 nm probe laser from the 939 nm pump beams before the detector are not perfect and that the detector was picking up a 939 nm signal, this lead to imprinting of the Doppler-broadened raw absorption signal on our lock-in signal. This, which contains in-homogeneous broadening, we feared could introduce a systematic shift in our measurements; using a narrow band pass filter has allowed us to circumvent this problem as the filter screws directly onto the detector and does not allow 939 nm light to pass through.

In March, we began systematically taking data using a ^{208}Pb and a ^{206}Pb/^{207}Pb vapor-cell. We took data measuring the transition isotope shift of both the 939 nm E2 and 406 nm E1 transitions between ^{206}Pb and ^{208}Pb, as well as the ^{207}Pb hyperfine constant. Much of our data differed from run to run, with different values from up and down scans within the same run, and enough scatter to indicate a larger problem. We re-aligned the laser's external cavity alignment, and found the small adjustment to cause drastic improvement in the laser's stability and our signal-to-noise ratio. We have since then been collecting data, providing the preliminary measurements in the next section used to analyze any potential systematic errors.

4.2 Data & Fitting

This section describes the process by which the raw spectroscopic data is processed and fitted to extract the desired measurements of transition isotope shifts and hyperfine constants for ^{207}Pb. The core of the analysis involves calibrating the frequency axis of the laser scan using a Fabry-Pérot cavity and fitting the observed spectroscopic signals using appropriate line-shape models.

Linearizing the Fabry-Pérot Signal

The LabVIEW data acquisition program simultaneously records the voltage corresponding to the ramp used to scan the probe laser frequency, the transmission signal from the Fabry-Pérot (FP) cavity, the raw probe laser transmission signal, and the Doppler-free absorption signal output by the Lock-in Amplifier. While the voltage ramp progresses linearly in time or point number, the frequency output of the (ECDL) probe laser does not necessarily change linearly. The non-linearities throughout the scan range are shown in Figure 4.1, highlighting the inherent non-linearity of the 406 nm scan laser frequency. To establish a linear frequency axis, against which we measure isotope shifts, the Fabry-Pérot cavity is used as a frequency reference. The FP cavity transmits light at resonant frequencies at constant value, separated by its Free Spectral Range. By observing the transmission peaks of the FP cavity during a laser scan, a series of markers is obtained at known frequency intervals.

The raw, non-linear, data can be mapped to a linear frequency axis, using the known separation of Fabry-Pérot transmission peaks. The relationship between the raw point number and frequency can be modeled by a polynomial; fitting this polynomial to the FP peaks allows the conversion of the non-linear point number axis to a relative linear frequency axis. Data is first normalized by dividing by the maximum value, then normalize the index points such that the x-axis spans from -1 to 1. Using the positions of the Fabry-Perot transmission peaks and the fact that the phase between consecutive peaks is π, phase values are assigned to the normalized FP peak locations. We perform a polynomial fit between the peaks, or pairs of peaks when the EOM is being used, normalized peak locations, and phase values. The coefficients of each scan's polynomial effectively define a mapping from the experimental x-axis scale to a linear phase scale. A non-linear model function is then created using Airy functions that take our polynomial as their argument, and can thus find exactly where any scanned data point lies in frequency relative to any other point.

Fitting the Experimental Data

Once the frequency axis has been linearized using the Fabry-Pérot signal, the experimental data can be mapped in frequency and thus fitted to extract the shifts between each isotope.

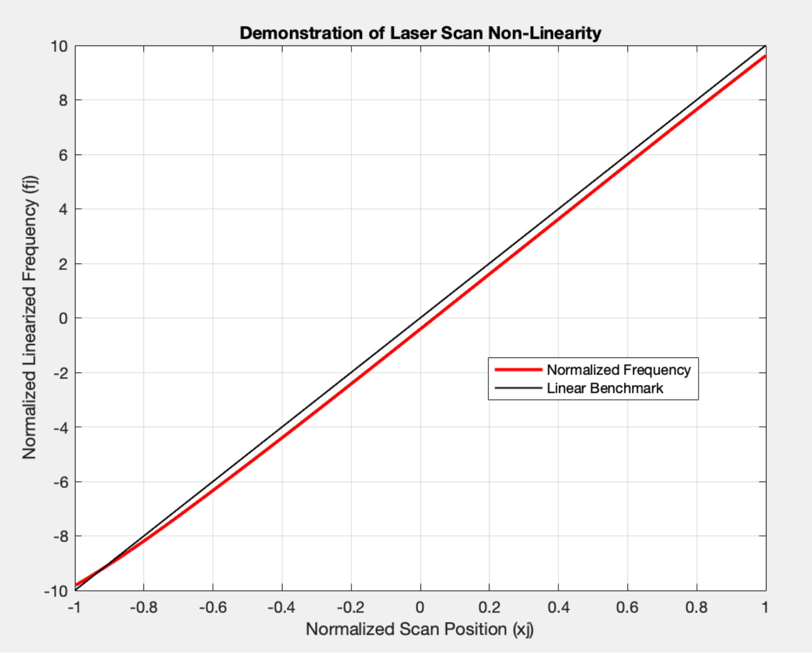

(a)

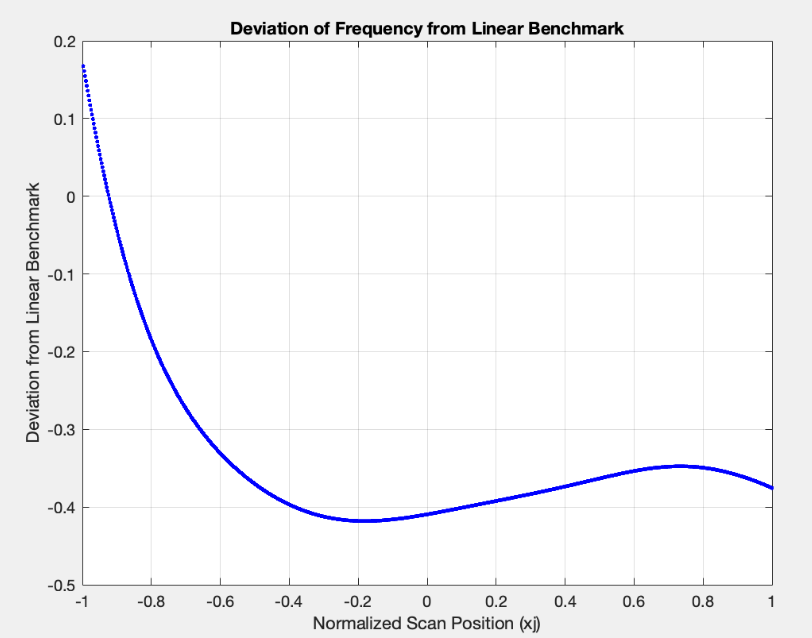

(b)

Figure 4.1: (a) The red line plots the normalized frequency against the normalized scan position. The normalized scan position represents the progression through the laser scan, analogous to the raw data point index. The solid black line represents a linear benchmark, indicating what a perfectly linear frequency scan with respect to scan position would look like. (b) The y-axis directly quantifies the magnitude of the non-linearity at each point in a single scan. The plot shows how much the calibrated frequency deviates from a perfectly linear sweep across the range of scan positions. The extent of this deviation in the laser scan highlights the need for linearization.

As discussed in Section 3.2, our method yields a narrow, Doppler-free signal with a Lorentzian lineshape, characteristic of homogeneous broadening mechanisms like natural lifetime and power broadening. Although collisions can cause re-thermalization, contributing a Gaussian shape, we modulate fast enough that there is no significant inhomogeneous shape to our signal.

We then fit to a sum of Lorentzians plus a linear background. Each Lorentzian peak corresponds to a specific atomic transition or, in the case of ^{207}Pb, a hyperfine component. The model is fitted to the measured transmission data, whose frequency axis was linearized using the Fabry-Pérot. The fit function for a sum of Lorentzians has the form:

$$\text{Signal}(f) = \text{Background}(f) + \sum_i A_i \frac{(\Gamma_i/2)}{(f - f_{0,i})^2 + (\Gamma_i/2)^2}$$

where A_i is the amplitude of the i-th peak, $f_{0,i}$ is its center frequency, and Γ_i is its Full Width at Half Maximum (FWHM). The fitting procedure adjusts the parameters (amplitudes, center frequencies, widths, and background parameters) from initial estimates to best match measured data. The primary parameters of interest are the center frequencies ($f_{0,i}$) of the observed peaks for each isotope.

Because we use both a co-propagating and a counter-propagating pump beam, each transition for a given isotope appears as two peaks in the spectrum, shifted in frequency due to the residual Doppler effect corresponding to each velocity class selected by the pump laser. The true transition frequency and the contribution from the first-step transition can be extracted from the measured frequencies of these two peaks with the equations presented in Section 3.2.

The fit code[1] takes the fitted center frequencies of the co- and counter-propagating peaks for different isotopes and applying formulas derived from equations 3.3 and 3.4 calculates the transition isotope shifts for both the 406 nm and 939 nm transitions. For ^{207}Pb, the fitting process is extended to identify multiple peaks corresponding to the hyperfine structure, and the differences in their center frequencies are used to determine the hyperfine constant.

Uncertainties for the calculated shifts and constants are estimated based on the errors in the fitted peak positions and the uncertainty in the FSR. This fitting and analysis process can be performed on multiple data scans by our fit code to obtain the final preliminary measurements reported in this thesis. Figure 4.2 is an example of the fitting process for a single up-scan. This scan took 10 seconds to collect and yields uncertainties of 1% or less in the TIS. Data is typically collected for 10 minutes at a time, yielding 50-55 scans (each including an up- and a down-scan); to date, nearly thirty such batches have been collected. Figure 4.3 shows the scatter between batches collected on a given day; in Figure 4.3 the up- and down-scans are highlighted to show their agreement. We have amassed approximately four hours of data from which both the 406 nm and 939 nm transition isotope shifts are measured for the even isotopes at under 1 MHz uncertainty. Preliminary measurements are presented in the next section.

---

[1] Provided in Appendix C

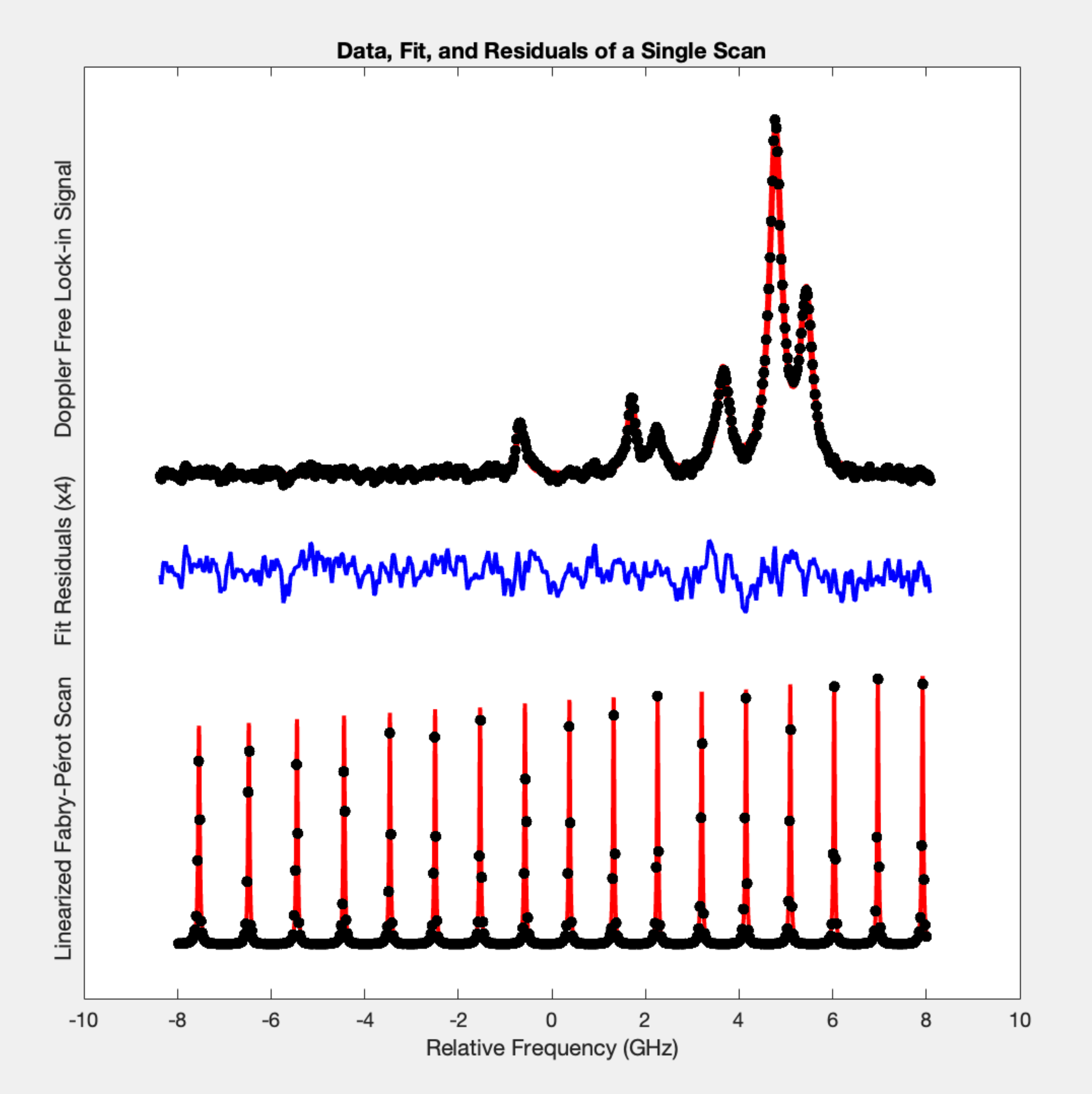

Figure 4.2: Bottom: Linearized Fabry-Pérot Scan. Top: Fitted transition isotope shift data. There are six Lorentzians: an absorption peak from both the co- and counter-propagating pump beam for each isotope. Middle: Residuals from the experimental data fit.

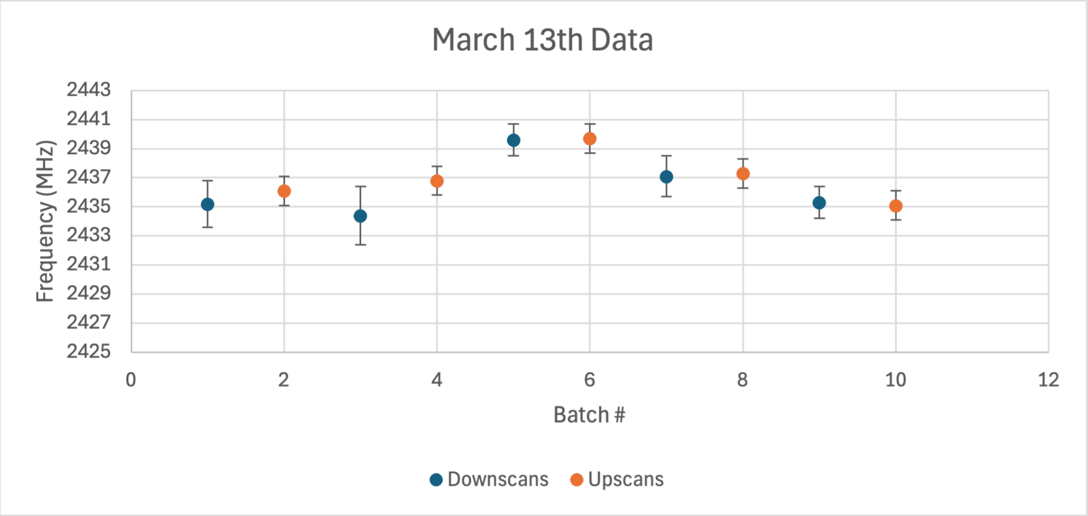

Figure 4.3: All data taken on March 13th for the lead 206-208 406 nm TIS. The experimental conditions for each batch can be found in Appendix B. Up and Down scans are highlighted to show agreement. Temperature, chop frequency, and laser power have been varied between batches. This data was taken using a mixed 206/207 and a pure lead 208 cell.

4.3 Preliminary Results

Tables 4.1 and 4.2 below summarize our measurements of transition isotope shifts as well as corresponding values from the literature.

Table 4.1: Isotope Shifts for the 406 nm (E1) Transition in Lead

Isotope Pair	**Measured Shift [MHz]**	**Literature Value [MHz]**
$^{204}\text{Pb} - ^{208}\text{Pb}$	4592.2(3)	4587.6(6)
$^{206}\text{Pb} - ^{208}\text{Pb}$	2437.4(4) & 2426.0(4)	2427.7(5)

Table 4.2: Isotope Shifts for the 939 nm (E2) Transition in Lead

Isotope Pair	**Measured Shift [MHz]**	**Literature Value [MHz]**
$^{204}\text{Pb} - ^{208}\text{Pb}$	374.8(1)	375.6(40)
$^{206}\text{Pb} - ^{208}\text{Pb}$	200.3(1) & 203.8(1)	200.7(30)

Although it has not been the focus of prior discussion, we also measured the ^{207}Pb hyperfine constant. Measuring the hyperfine constant is in reality the same method as measuring isotope shifts, but rather than measuring small shifts in energy (of isotope shifts) we measure small energy shifts between hyperfine levels. Our preliminary measurement for the hyperfine constant of ^{207}Pb shown in Table 4.3

Table 4.3: Hyperfine Constant for Lead-207

Measurement Type	**Measured Hyperfine Constant [MHz]**	**Literature Value [MHz]**
^{207}Pb $^3P_2$ Hyperfine Constant	2604.6(3)	2600.8(9)
^{207}Pb $^3P_1$ Hyperfine Constant	8813.7(5)	8802.0(16) & 8807.2(30)

4.4 Error Analysis

During the analysis of preliminary data we considered potential systematic errors. Data collected on March 13th[2] consisted of twelve batches of data, each with at least fifteen up and down scans, systematic variation of temperature, chopping frequency, and laser power.

Temperature

Temperature, in theory, does not affect the transition isotope shift. We have been able to detect signals as temperatures low as 700°C and have taken data with temperature as high as 850°C. As expected, no significant differences in transition isotope shifts were observed across different temperatures.

Chopping frequency

Section 2.4 considered how our signal, rather than being a convolution, is a superposition of a Gaussian (from inhomogeneous Doppler-broadening) and a Lorentzian (from homogeneous broadening mechanism); chopping frequency, which dictates how many atoms we interact with, and if they have enough time to collide and re-thermalize impacts our lineshape. Increasing chopping frequency decreases the Gaussian contribution to lineshape. Data taken at frequencies between 500kHz and 1.5MHz, show no notable differences.

Laser Power

Laser power can contribute to line broadening. The transitions we have analyzed so far are E1 and E2 transitions, both of which are relatively weak. Given the weakness of these transitions and the available laser power, our primary concern is maximizing laser intensity rather than mitigating power broadening or Stark shifts.[3]. However, we have still taken data with various degrees of attenuation, and verified that laser power does not affect our measurement.

---

[2] A list of this data is tabulated in Appendix B

[3] When atoms interact with a strong laser field, the electromagnetic radiation can induce a periodic electric field perturbing an atom's energy levels; this perturbation can cause the energy levels to shift.

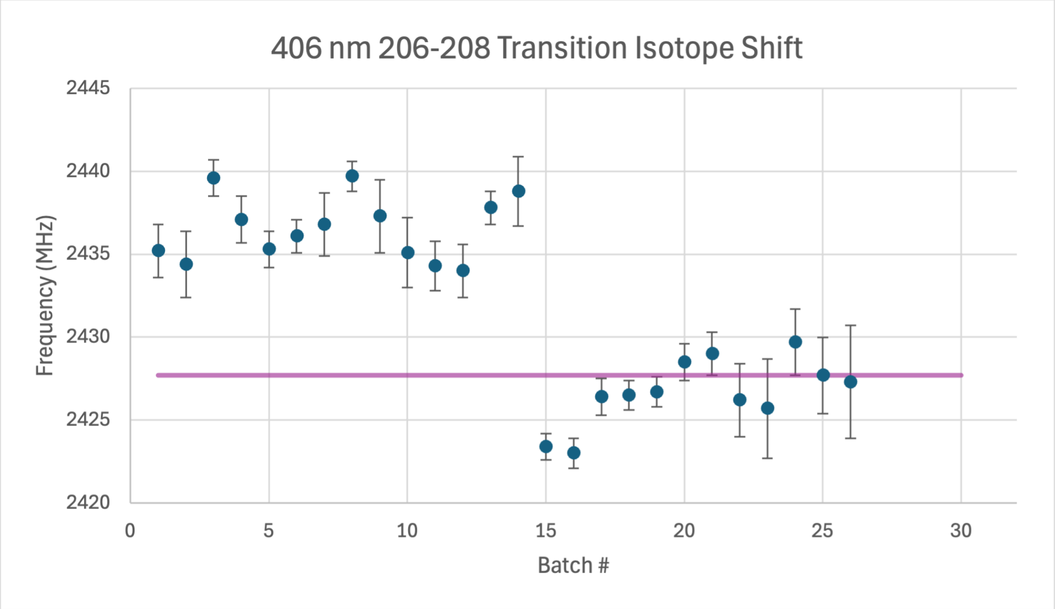

Figure 4.4: A comparison of all of our data for the 406 nm 206-208 Transition Isotope Shift, the previous measurement by [8] is shown in purple.

Scan Direction

A probe laser scans in frequency. For the purposes of this experiment, scans range over 10 MHz. In principle, scan direction, whether the laser is scanning up or down, has no impact on measurements in this experiment. However, when a laser is not scanning properly or is having stability problems, it is not uncommon to observe a systematic difference in measured value between up and down scans; this was a problem faced by Abby Kinney 24' in [16]. We don't see any systematic discrepancy between up and down scans in this experiment; this can be seen in Figure 4.3, where batches of up and down scans have been highlighted.

Systematic Error

We've discovered a systematic error, which needs further exploration. Data collected in March was taken using a pure 208 cell and a 206/207 mixed cell. After analyzing this data, the samples within the furnace were changed to three cells in series: a 204/207 mixed cell and pure 206 and 208 cells. The vapor cells used should not affect the measurement, as cells should contain only lead, and the chopping rate is faster than the rate of collisions. This configuration (with all three even isotopes) allows measurement of all the transition isotope shifts for both the 1st and 2nd step transitions in a single experiment. When comparing data from before and after changing samples, a systematic shift is noted in the measured value, shown in Figure 4.4. There is a clear shift in measurements between batches 14 and 15 in Figure 4.4. The first batch after changing the vapor cells was in agreement with the data taken beforehand, but afterward, with still good precision, different values were measured, where both values are well outside the reasonable range of uncertainty. We have theories about what could be the source of this error. Our suspicion is the mixed cell environment. We believed that at our modulation frequency, it would not matter if mixed lead samples were used, and that it was advantageous to use these cells as multiple isotopes were guaranteed to be in identical environments. The most blatant difference between the set-up that these disagreeing measurements came from was that one used a mixed 206/207 cell and the other a pure 206 cell[4]. We plan to investigate whether mixed versus pure cell environments change our measurement. The lock-in amplifier is phase-dependent and thus must be phase-optimized before taking a measurement; if done incorrectly, this may lead to a distortion of our lineshape and could potentially lead to a shift in measurement. We plan to systematically investigate the effect of lock-in amplifier phase optimization on the fitted value. The third thing we plan to investigate is the probe laser scan quality. We have shifts in measured value from batches where the laser is scanning poorly; there is no noticeable indication in our Fabry-Pérot data that the laser was scanning poorly during this period of time (about 10 Days), but we are exploring it anyway.

4.5 Discussion

Our measurement is not only the first direct measurement of the 930 nm transition isotope shift, but is in agreement with the experimentally inferred literature value (which is an order of magnitude less precise). However, some of our measurements of the 406 nm transition isotope shift are in disagreement with the literature; our measurements have had as high as a 0.37% disagreement and can lie far outside the uncertainty of the measurement made in 2000 [8]. Their measurement is a one-step saturated absorption spectroscopy experiment, like the one described in Section 2.5. The crucial difference between our experiments lies in the generation of the atomic vapor. Bouazza et al. use cathode discharge to produce a plasma containing lead atoms in metastable states, whereas our experiment employs an evacuated furnace to create a lead vapor in thermal equilibrium characterized by a well-defined Boltzmann distribution of atomic states. While both methods successfully achieve a sufficient population of the lower level of the 406 nm transition, our thermal vapor allows for a more straightforward application of the Boltzmann distribution to understand the initial state populations, where the plasma environment may involve more complex excitation and ionization processes. We do not assert that one method is correct and the other not, despite differences in methodology; both approaches enable high-resolution Doppler-free measurements, we do not find a disagreement with previous methods troublesome, we need further data to make a conclusion, and do not allowing a past measurement to influence our findings.

Our measurement of the hyperfine constant warrants discussion as well. To measure the

---

[4] In both cases, the same pure 208 cell was used.

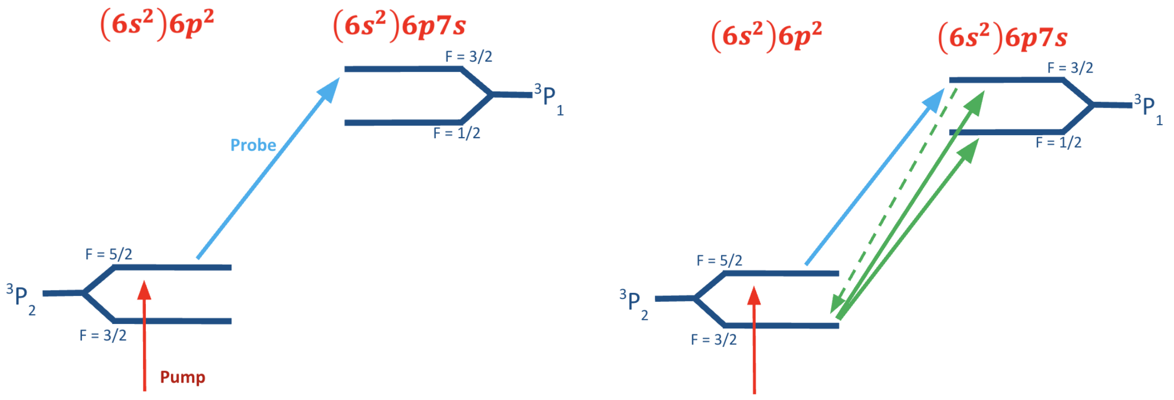

(a) (b)

Figure 4.5: Energy level diagrams of the $6s^2 6p^{23}\mathrm{P}_2$ and $6s^2 6p7s^3\mathrm{P}_1$ hyperfine splitting. (a) shows the ${}^3\mathrm{P}_2$ 5/2 → ${}^3\mathrm{P}_1$ 3/2 transition we are explicitly driving by tuning the pump laser to the ${}^3\mathrm{P}_2$ 5/2 state. (b) shows the decay down to the ${}^3\mathrm{P}_2$ 3/2 in green (dotted) and the then possible transitions from that state in green(solid).

hyperfine splitting, we originally tuned our 939 nm pump laser to drive atoms from the ground state to the $f = 5/2$ upper-level hyperfine level of the intermediate state, then using the 406 nm probe laser we expected to see two absorption peaks, the ${}^3\mathrm{P}_2$ 5/2 → ${}^3\mathrm{P}_1$ 3/2 transition depicted in blue in Figure 4.5b and the weaker ${}^3\mathrm{P}_2$ 3/2 → ${}^3\mathrm{P}_1$ 3/2 transition in green. The lifetime of the ${}^3\mathrm{P}_1$ 3/2 state is short enough that it can decay down to the ${}^3\mathrm{P}_2$ 3/2 state and be driven up to the ${}^3\mathrm{P}_1$ 3/2 while the probe beam is scanning up in frequency. This is not what we observed, rather, we saw three absorption peaks: the two we expected, as well as the ${}^3\mathrm{P}_2$ 3/2 → ${}^3\mathrm{P}_1$ 1/2, in principle, this transition can be driven in exactly the same way as the ${}^3\mathrm{P}_2$ $3/2 \rightarrow^3$ P_2 3/2 where the lower state is populated by decay from the transition we are directly driving, however, this transition happens in the scan *before* we drive the ${}^3\mathrm{P}_2$ 5/2 → ${}^3\mathrm{P}_1$ 3/2 transition whose decay would permit that transition; implying that state is being populated by decay from a state we hadn't populated yet, which would could not have been possible.

We have not yet fully investigated this phenomenon, but our working theory is inspired by Purcell and Field's 1956 paper on the "Influence of Collisions upon Population of Hyperfine States in Hydrogen" [17]; in which they find that collisions in hydrogen can result in exchanged electron orientation. Which could account for how we are somehow populating the ${}^3\mathrm{P}_2$ 3/2 state in the same velocity class with the same modulation frequency we drive the AOM at without pumping the state directly. If such collisions exist within our method we belive this could explain why our measurement using a mixed cell disagrees with ours taken in a pure cell.

Chapter 5

Future Work

This section discusses the future work to be done in completing this experiment. The first section discusses the three even isotopes and the pair of transitions discussed by this thesis, the second is focused on another pair of transitions. Finally, our plan for measuring the isotope shifts in ^{207}Pb is discussed.

5.1 Even Isotopes and the 406/939 nm Transitions

As mentioned in Section 4.4, we have discovered a potential systematic error in our experiment, which could lead to a shifted measurement. Any dependence of our measurement on chopping frequency, temperature, or laser power has been eliminated, but we still have an error to explore. Our preliminary measurements had an uncertainty of less than a MHz, from around a thousand scans; our statistical uncertainty decreases with $1/\sqrt{n}$, so this uncertainty can be addressed with additional data, once our systematic error is further investigated.

5.2 The 368/1279 nm Transitions

This thesis has focused on the 939 and 406 nm transitions. Figure 5.1 below is a modified version of Figure 1.1 highlighting another similar pair of transitions the: $6s^26p^2$, $^3P_0$ to $^3P_1$ 1279 nm M1 transition, and the $6s^26p^2$ $^3P_1$ to $6s^26p7s$ $^3P_1$ 368 nm E1 transition. The experimental method used in this thesis could be applied to measuring the transition isotope shifts of these transitions as well.

Conceptually, there is no significant difference between these pairs of transitions, and therefore the two-step Doppler-free scheme is also able to measure these transition isotope shifts. We have a 368 nm UV home-built laser, as well as a commercial 1279 nm laser; the AOM used for modulation in this thesis can modulate the 1279 nm laser. Most importantly, we have achieved a Doppler-free two-step signal from these lasers to verify that the method described here is also applicable to these transitions.

There are, however, a few practical matters that need to be considered. Principally,

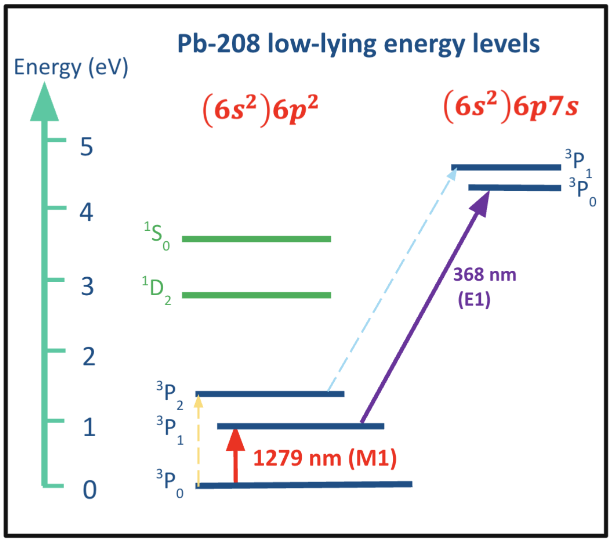

Figure 5.1: The low-lying energy levels of lead, with the 368 and 1279 nm in bold. The transitions discussed throughout the rest of the thesis are dotted for reference.

the wavemeter we use to lock the 939 nm, will not work at 1279 nm, nor can we modulate the UV laser with an EOM for frequency modulation, in the same way we do for the 406 nm laser. Julia Matin '25 has successfully locked the pump laser using a Proportional–Integral–Derivative (PID) controller, and more information can be found in her Independent Study Report. While we have demonstrated that these isotope shifts can be measured, it will require additional development beyond a simple change of lasers.

5.3 Measurement of ^{207}Pb Isotope Shifts

This section outlines the plan to measure the isotope shifts in ^{207}Pb; the presence of an odd number of neutrons in this isotopes' nucleus gives rise to hyperfine splitting. The measurement of ^{207}Pb transition isotope shifts builds on our current two-step excitation scheme. We still use a modulated pump laser to excite lead atoms to an intermediate state, followed by a probe laser to further excite them to a higher energy level. However, to specifically address the hyperfine structure of ^{207}Pb (nuclear spin $I = 1/2$) and its transition isotope shift relative to even isotopes, we will employ an optical fiber-based tunable Electro-Optic Modulator (EOM). This EOM, identically to the one we use for frequency calibration, generates sidebands, only now on the first-step laser (939, 1279 nm), this EOM however is tunable so the frequency separation between each higher-order peak can be set by a function generator. In our application the EOM sidebands will be tuned in frequency to match the energy splitting between the even isotope peak and each of the ^{207}Pb hyperfine components, from which we can extract the shift of the center of ^{207}Pb from any of the even is isotopes we have already measured. Further details regarding the specific methodology and modifications to the experimental apparatus for measuring ^{207}Pb transition isotope shift with the use of the tunable fiber-based EOM can be found in Appendix B.

Appendix A

Measuring ^{207}Pb TIS

A.1 Measuring ^{207}Pb TIS

This appendix outlines the methodology for measuring the transition isotope shifts (TIS) for the odd lead isotope, ^{207}Pb. This measurement builds upon the two-step Doppler-free spectroscopy scheme developed for the even isotopes of lead and described in this thesis.

A.2 The Problem with ^{207}Pb

Measuring the TIS for isotopes with nuclear spin, such as ^{207}Pb (which has a nuclear spin I = 1/2), presents an additional challenge compared to the even isotopes (^{204}Pb, ^{206}Pb, ^{208}Pb) which have no nuclear spin. The presence of nuclear spin in odd isotopes gives rise to hyperfine splitting (HFS), where atomic energy levels are split into multiple sublevels due to the interaction between the nuclear magnetic dipole moment (and higher-order moments) and the magnetic fields produced by the atomic electrons.

For even isotopes, a specific electronic transition corresponds to a single absorption peak in our spectrum. The TIS between two even isotopes is simply the difference in the central frequency of these single peaks for the respective isotopes. However, for ^{207}Pb, the same electronic transition is split into multiple hyperfine components. Therefore, the concept of TIS for ^{207}Pb relative to an even isotope refers to the shift of the center, the frequency that hyperfine splitting shift above and below, of the ^{207}Pb hyperfine structure from the central frequency of the even isotope peak.

While measuring the hyperfine constant itself is methodologically similar to measuring isotope shifts, focusing on energy differences between hyperfine levels rather than between isotopes, determining the overall TIS of the ^{207}Pb structure relative to even isotopes requires a modification of our standard approach. A significant practical challenge is that the frequencies corresponding to the ^{207}Pb hyperfine component transitions in the first excitation step (939 nm or 1279 nm) are often located well outside the Doppler envelope that encompasses the even isotope transitions in our heated vapor cell. The standard Doppler-free technique, which relies on optically pumping a narrow velocity class within the Doppler-broadened profile, would not directly access these far-detuned hyperfine transitions efficiently when the pump laser is tuned near the even isotope resonances.

A.3 Proposed Method using a Tunable Fiber-Based EOM

To overcome the challenge of measuring the ^{207}Pb TIS relative to the even isotopes, we propose a method that modifies our two-step excitation scheme using a tunable fiber-based Electro-Optic Modulator (EOM). The fundamental two-step process remains the same: a first-step (pump) laser excites atoms to an intermediate state ($^3P_2$ via the 939 nm transition), and a second-step (probe) laser further excites them to a higher energy level (6s^{2}6p7s $^3P_1$ via the 406 nm transition). The difference is the introduction of a tunable fiber-based EOM into the path of the pump laser. This EOM, similar in principle to the one used for frequency calibration, generates sidebands of integer multiples of the driving frequency shifted from the main laser frequency; only using a tuneable-fiber-based EOM The frequency separation of these sidebands can be precisely controlled by a function generator driving the EOM.

In Figure A.1, the horizontal axis represents frequency. Vertical lines denote the center frequencies of specific atomic transitions. The line labeled "208" indicates the single transition frequency for ^{208}Pb isotope. ^{207}Pb energy levels are split into hyperfine components.

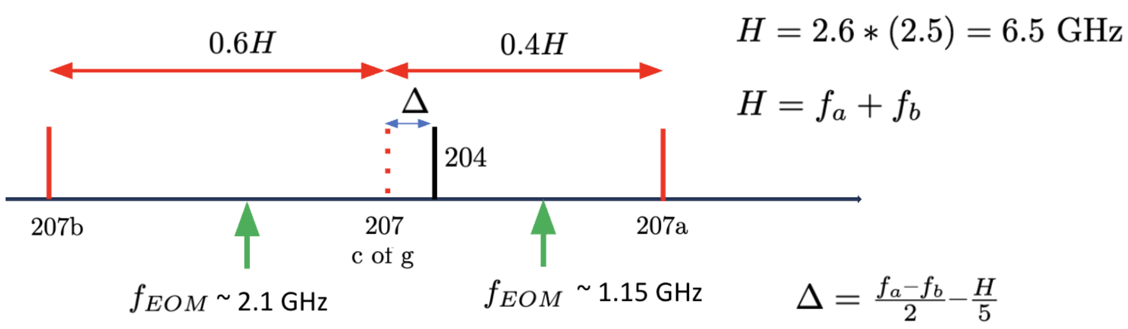

f_a, f_b are the averages of the CO and CTR for each hyperfine component

Figure A.1: An example of this method for ^{204}Pb and ^{207}Pb, and the 939 nm and 406 nm transition pair.

The lines labeled "207b" and "207a" represent two specific hyperfine components of ^{207}Pb for the 939 nm transition. "207 c of g" indicates the calculated "center of mass" or average position of the ^{207}Pb hyperfine components '207b' and '207a' from which it's transition isotope shift is measured. The red arrows labeled "0.4 H" and "0.6 H" show the relative frequency separation of the '207a' and '207b' hyperfine components with respect to the '207 c of g'. The total frequency separation between '207b' and '207a' is defined as H. $H = 2(f_a + f_b)$ defines the total splitting H, where f_a and f_b are frequencies related to the hyperfine components. The hyperfine constant A can be calculated using A $= (4/5)(f_a + f_b)$ for the 939 nm transition. The transition isotope shift Δ, can be calculated as $\Delta = (f_a - f_b)/2 - H/5$. Δ represents the transition isotope shift (TIS) between the ^{204}Pb resonance and the '207 c of g'. f_{EOM} indicate the frequencies at which an Electro-Optic Modulator (EOM) is operated. This EOM, which is tunable and can create this frequencies with a function generator and amplifier.

Appendix B

A Tabulation of Preliminary Data

Table B.1: Experimental Run Parameters for Lead Spectroscopy

Date	**FSR (MHz)**	**Temp. (°C)**	**Chop Freq. (MHz)**	**Cells**	**Power**
13-Mar	999.7	800	1.5	206/207+208	P0
13-Mar	999.7	800	1.5	206/207+208	P0
13-Mar	999.7	850	1.5	206/207+208	P0
13-Mar	999.7	850	1.5	206/207+208	P0
13-Mar	999.7	750	1	206/207+208	P0
13-Mar	999.7	750	1	206/207+208	P0
13-Mar	999.7	700	0.5	206/207+208	P0
13-Mar	999.7	700	0.5	206/207+208	P0
13-Mar	999.7	850	1.5	206/207+208	P0/2
13-Mar	999.7	850	1.5	206/207+208	P0/2
13-Mar	999.7	850	1.5	206/207+208	P0/4
13-Mar	999.7	850	1.5	206/207+208	P0/4
11-Apr	999.4	830	2	206+208+204/207	P0
11-Apr	999.4	830	2	206+208+204/207	P0
11-Apr	999.4	830	2	206+208+204/207	P0
11-Apr	999.4	830	2	206+208+204/207	P0
14-Apr	999.5	850	1	206+208+204/207	P0
14-Apr	999.5	850	1	206+208+204/207	P0
14-Apr	999.5	850	1	206+208+204/207	P0
14-Apr	999.5	850	1	206+208+204/207	P0
17-Apr	999.6	850	1	206+208+204/207	P0
17-Apr	999.6	850	1	206+208+204/207	P0
21-Apr	999.8	850	1	206+208+204/207	P0
21-Apr	999.8	850	1	206+208+204/207	4P0/5
21-Apr	999.8	850	1	206+208+204/207	4P0/5

Date	**FSR (MHz)**	**Temp. (°C)**	**Chop Freq. (MHz)**	**Cells**	**Power**
21-Apr	999.8	850	1	206+208+204/207	P0/5
21-Apr	999.8	850	1	206+208+204/207	P0/5
21-Apr	999.8	850	1	206+208+204/207	P0/5

Appendix C

Fit Codes

The first code was developed to separate the Up and Down scans into their own .txt file. Historically, this was done by hand, but with the development of this code during this thesis, we can now process what used to take hours in minutes. The second is for the Fabry-Pérot Cavity, which can fit both with and without the higher-order side bands by commenting/uncommenting out the indicated lines. The EOM sideband fits are quite sensitive to initial guesses, we've found success fitting a batch without the EOM to get initial guesses for the EOM fit. The third is the complete fit code, it completes and outputs the measurement of all the even isotope shifts, but can be easily modified to work with fewer isotopes or to fit the hyperfine constant.

Note: All fit codes are also available in the Majumder Lab Drive in the folder titled "Fit Codes" in my thesis folder.

C.1 Up-scan Down-scan Separator

This code, when run, splits a *.lvm* into separate .txt files for each up and down scan in the same folder. The first and last scans, if incomplete, are automatically removed.

```
rawdata=sprintf("Data_12_April_850C_1MHz_Scan1.lvm");
Data=importdata(rawdata);

n=Data(:,2);
TTL=Data(:,3);
FP=Data(:,4)
Transmission=Data(:,6);
Spectrum=Data(:,5);

numRows = size(n);
ReducedScan = TTL(1:1:numRows,:);
```

```

loc1=[];
loc2=[];
for i=2:numRows

if TTL(i)-TTL(i-1)>2
    loc1=[loc1;i];
else

 if TTL(i)-TTL(i-1)<-2
     loc2=[loc2;i];
 else
     0;
 end
end
end


UpScanPos=loc1;
DownScanPos = loc2;

%reducing frequency to find upscan and downscan locations in Scan
[NumberUpScans, i1] = size(UpScanPos);
[NumberDownScans, i2] = size(UpScanPos);
NumberScans = NumberDownScans + NumberUpScans -1;
Locations = [UpScanPos(:);DownScanPos(:)];
Locations = sort(Locations);

UpscanOutput=zeros(1);
DownscanOutput=zeros(1);
plot(Spectrum)
UpScanCounter = 0;
DownScanCounter = 0;

for i=1:1:NumberScans

    if(ismember(Locations(i,:),DownScanPos))
        UpScanCounter = UpScanCounter+1;
        UpscanOutput=[n(Locations(i)-Locations(i)+2:Locations(i+1)-Locations(i)+2),FP(Locations(i):Locations(i+1)),Spectrum(Locations(i):Locations(i+1)),Transmission(
```

```
            Locations(i):Locations(i+1))];
        writematrix(UpscanOutput,sprintf("UpscanTISData0%02d.txt",UpScanCounter))
    else
        DownScanCounter = DownScanCounter+1;
        DownscanOutput=[n(Locations(i)-Locations(i)+2:Locations(i+1)-Locations(i)+2),FP(Locations(i):Locations(i+1)),Spectrum(Locations(i):Locations(i+1)),Transmission(Locations(i):Locations(i+1))];
        writematrix(DownscanOutput,sprintf("DownscanTISData0%02d.txt",DownScanCounter))
    end

 end
```

C.2 Fabry-Pérot Fit Code

This code fits the Fabry-Pérot data both with and without an EOM. Switching between the two versions requires swapping line 36 for 37 and 40 for 42. We have found success fitting data from a batch without the EOM to get the initial guesses to be used as parameters five through eleven in the initial guess vector "*beta*0".

```
1  NoScans=2;
2  
3  FSRguess=1;
4  p=pi;
5  FreeSpectralRange=zeros(1);
6  EFSR=zeros(1);
7  shave=0;
8  
9  
10 for n = 1:NoScans
11     UpscanDataFileON = sprintf("UpscanTISData0%02d.txt",n);
12     % UpscanDataFileON = sprintf("DownscanTISData0%02d.txt",n);
13     Data=importdata(UpscanDataFileON);
14     % Data=flip(importdata(UpscanDataFileON));
15 
16     %Defining arrays from LabVIEW measurement file for upscans with field ON
17 size=length(Data);
18 PointNo=[shave+1:size];
19 FP=(Data(shave+1:size,2))/max(Data(shave+1:size,2));
```

```


%Normalises the x axis to be between -1 and 1
xj=((PointNo-shave)-((length(PointNo))/2))/((length(PointNo))
  /2);

%Plots the different isotope data and the Fabry-Perot data
  against xj

[pks,locs]=findpeaks(FP,'MinPeakHeight',0.3);
warning('off','all')
warning

order=7;
xlocs=(locs-length(Data)/2)/(length(Data)/2);
phase=[-round((length(xlocs)-1)/2):round((length(xlocs)-2)/2)]*
  pi;
polyparms=flip(polyfit(xlocs,phase,order-1));

%beta0=[0.00 1.0 0.01 200 polyparms];
beta0=[0.00 1.0 0.01 100    2.3871  30.5933  -2.7755 0.2397
  -0.7751 -0.8659  0.8445 0.5 0.6 0.5 0.0 0.0];


%FPModel=@(b,x) b(1)+(b(2)+b(3).*x).*(1+b(4)*(sin((b(5)+b(6)*x+
  b(7)*x.^2+b(8)*x.^3+b(9)*x.^4+b(10)*x.^5+b(11)*x.^6))).^2)
  .^(-1);

FPModel=@(b,x) b(1)+(b(2)+b(3).*x).*(1+b(4)*(sin((b(5)+b(6)*x+b
  (7)*x.^2+b(8)*x.^3+b(9)*x.^4+b(10)*x.^5+b(11)*x.^6))).^2)
  .^(-1)...
   +b(12).*(b(2)+b(3).*x).*(1+b(4)*(sin((b(5)+1.*(pi/FSRguess)
     .*b(13)+b(6)*x+b(7)*x.^2+b(8)*x.^3+b(9)*x.^4+b(10)*x.^5+
     b(11)*x.^6))).^2).^(-1)...
   +b(14).*(b(2)+b(3).*x).*(1+b(4)*(sin((b(5)-1.*(pi/FSRguess)
     .*b(13)+b(6)*x+b(7)*x.^2+b(8)*x.^3+b(9)*x.^4+b(10)*x.^5+
     b(11)*x.^6))).^2).^(-1)...
  +b(15).*(b(2)+b(3).*x).*(1+b(4)*(sin((b(5)+1.*2.*(pi/
    FSRguess).*b(13)+b(6)*x+b(7)*x.^2+b(8)*x.^3+b(9)*x.^4+b
    (10)*x.^5+b(11)*x.^6))).^2).^(-1)...
   +b(16).*(b(2)+b(3).*x).*(1+b(4)*(sin((b(5)-1.*2.*(pi/
     FSRguess).*b(13)+b(6)*x+b(7)*x.^2+b(8)*x.^3+b(9)*x.^4+b
```

```
        (10)*x.^5+b(11)*x.^6))).^2).^(-1);
%FP fitting function

figure
plot(xj,FP,'k.','MarkerSize',15)
hold on
plot(xj,FPModel(beta0,xj),'LineWidth',2.3)
hold off

mdl=fitnlm(xj,FP,FPModel,beta0);
beta0 = mdl.Coefficients.Estimate
mdl.Coefficients.SE;

%FSR=FSRguess;
FSR=(0.6/beta0(13)).*FSRguess;
%UncFSR=0;

UncFSR=(FSRguess.*0.6./((beta0(13).^2)/pi)).*mdl.Coefficients.
   SE(13);

fj=FSR*(1/pi)*(beta0(5)+beta0(6).*xj+beta0(7).*(xj).^2+beta0(8)
   .*(xj).^3+beta0(9).*(xj).^4+beta0(10).*(xj).^5+beta0(11).*(
   xj).^6);
xdata=linspace(-1.,1.,5000);

figure
plot(xj,FP,'k.','MarkerSize',15)
hold on
plot(xdata,FPModel(beta0,xdata),'LineWidth',2.3)
hold off
%plots the FP fit against xj showing data and fit

figure
plot(fj,mdl.Residuals.Raw,"r.-","LineWidth",2)
hold off

FPQuality=dot(mdl.Residuals.Raw,mdl.Residuals.Raw)/(size-shave
   -1)



fprintf('\n The Free Spectral Range is %.1f +/- %.1f MHz',
```

```
   1000.*FSR,1000.*UncFSR)

FreeSpectralRange(n)=FSR;
EFSR(n)=UncFSR;

end


%[FreeSpectralRange',EFSR']
```

C.3 Transition Isotope Shift (& Hyperfine constant) Fit Code

Similarly, this code fits the experimental data and outputs the transition isotope shifts between the even isotopes. By un-commenting certain lines and commenting others out, it can be easily adapted to fit the HFS of ^{207}Pb.

```
close all;
scan1 =1;
NoScans=5;

FSRguess=0.9998;

kB=1.38*10^-23; %Boltzmann constant
T=850+273; %Temperature
m208=208*1.66*10^-27;%Mass of 208
clight=299792458; %Speed of light
lambda=405.8*10^-9; %Wavelength
DopplerWidth=sqrt(kB*T*(m208*clight^2)^-1)*(clight/lambda)*10^-9; %This calculates the Doppler width
p=pi;
f939=319288.774;
f406=738595.6;

beta208=[0 1 -0.8 .1 1 1.5 1 2.1 1 3.4 0.1 0 .1 .1 4.7 .1 5.2];
%beta208=[0 1 -7.62 .1 1 -1.0 1 .1 .1 5.8];

TIS406206208=zeros(1);
ETIS406206208=zeros(1);
TIS939206208=zeros(1);
ETIS939206208=zeros(1);
```

```
TIS406204208=zeros(1);
ETIS406204208=zeros(1);
TIS939204208=zeros(1);
ETIS939204208=zeros(1);
HFC=zeros(1);
EHFC=zeros(1);
UHFC=zeros(1);
EUHFC=zeros(1);
FreeSpectralRange=zeros(1);
EFSR=zeros(1);
shave=0;


for n = scan1:NoScans
    UpscanDataFileON = sprintf("UpscanTISData0%02d.txt",n);
    Data=importdata(UpscanDataFileON);

    %Defining arrays from LabVIEW measurement file for upscans with field ON
size=length(Data);
PointNo=[shave+1:size];
Trans=((Data(shave+1:size,4))/max(Data(shave+1:size,4)));
Pb208=((Data(shave+1:size,3))/max(Data(shave+1:size,3)))./1;
FP=(Data(shave+1:size,2))/max(Data(shave+1:size,2));
% Pb208=Pb208./Trans;

%Normalises the x axis to be between -1 and 1
xj=((PointNo-shave)-((length(PointNo))/2))/((length(PointNo))/2);

%Plots the different isotope data and the Fabry-Perot data against xj

[pks,locs]=findpeaks(FP,'MinPeakHeight',0.4);
warning('off','all')
warning

order=11;
xlocs=(locs-length(Data)/2)/(length(Data)/2);
phase=[-round((length(xlocs)-1)/2):round((length(xlocs)-2)/2)]*pi;
polyparms=flip(polyfit(xlocs,phase,order-1));
```

```

beta0=[0.00 1.0 0.01 100 polyparms];
%beta0=[0.00 1.0 0.01 100 polyparms 0.1 0 0.1 0.1 0.1];


FPModel=@(b,x) b(1)+(b(2)+b(3).*x).*(1+b(4)*(sin((b(5)+b(6)*x+b(7)*x.^2+b(8)*x.^3+b(9)*x.^4+b(10)*x.^5+b(11)*x.^6+b(12)*x.^7+b(13)*x.^8+b(14)*x.^9+b(15)*x.^10))).^2).^(-1);

%FPModel=@(b,x) b(1)+(b(2)+b(3).*x).*(1+b(4)*(sin((b(5)+b(6)*x+b(7)*x.^2+b(8)*x.^3+b(9)*x.^4+b(10)*x.^5))).^2).^(-1)...
 %    +b(11).*(b(2)+b(3).*x).*(1+b(4)*(sin((b(5)+1.*b(12)+b(6)*x+b(7)*x.^2+b(8)*x.^3+b(9)*x.^4+b(10)*x.^5))).^2).^(-1)...
  %  +b(13).*(b(2)+b(3).*x).*(1+b(4)*(sin((b(5)-1.*b(12)+b(6)*x+b(7)*x.^2+b(8)*x.^3+b(9)*x.^4+b(10)*x.^5))).^2).^(-1)...
   %+b(14).*(b(2)+b(3).*x).*(1+b(4)*(sin((b(5)+1.*2.*b(12)+b(6)*x+b(7)*x.^2+b(8)*x.^3+b(9)*x.^4+b(10)*x.^5))).^2).^(-1)...
    %+b(15).*(b(2)+b(3).*x).*(1+b(4)*(sin((b(5)-1.*2.*b(12)+b(6)*x+b(7)*x.^2+b(8)*x.^3+b(9)*x.^4+b(10)*x.^5))).^2).^(-1);
%FP fitting function

mdl=fitnlm(xj,FP,FPModel,beta0);
beta0 = mdl.Coefficients.Estimate;
mdl.Coefficients.SE;

FSR=FSRguess;
%FSR=0.6./(beta0(12)./pi);
UncFSR=0;
%UncFSR=(FSRguess.*0.6./((beta0(12).^2)/pi)).*mdl.Coefficients.SE(12);

fj=FSR*(1/pi)*(beta0(5)+beta0(6).*xj+beta0(7).*(xj).^2+beta0(8).*(xj).^3+beta0(9).*(xj).^4+beta0(10).*(xj).^5+beta0(11).*(xj).^6+beta0(12).*(xj).^7+beta0(13).*(xj).^8+beta0(14).*(xj).^9+beta0(15).*(xj).^10);
xdata=linspace(-1.,1.,5000);

figure
plot(xj,FP,'k.','MarkerSize',15)
hold on
```

```
plot(xdata,FPModel(beta0,xdata),'LineWidth',2.3)
hold off
%plots the FP fit against xj showing data and fit

%figure
%plot(fj,mdl.Residuals.Raw,"r.-","LineWidth",2)
%hold off

FPQuality=dot(mdl.Residuals.Raw,mdl.Residuals.Raw)/(size-shave-1)

GaussFit=@(b,x) b(1)+(b(2)+b(12).*x).*(b(4)/(2.*pi))./((x-b(3)).^2+(b(4)/2).^2)...
   +b(5).*(b(4)/(2.*pi))./((x-b(6)).^2+(b(4)/2).^2)...
   +b(7).*(b(11)/(2.*pi))./((x-b(8)).^2+(b(11)/2).^2)...
   +b(9).*(b(11)/(2.*pi))./((x-b(10)).^2+(b(11)/2).^2)...
    +b(13).*(b(14)/(2.*pi))./((x-b(15)).^2+(b(14)/2).^2)...
    +b(16).*(b(14)/(2.*pi))./((x-b(17)).^2+(b(14)/2).^2);

%GaussFit=@(b,x) b(1)+(b(2)).*(b(4)/(2.*pi))./((x-b(3)).^2+(b(4)/2).^2)...
 %   +b(5).*(b(7)/(2.*pi))./((x-b(6)).^2+(b(7)/2).^2)...
  %  +b(8).*(b(9)/(2.*pi))./((x-b(10)).^2+(b(9)/2).^2);


figure
plot(fj,GaussFit(beta208,fj),"r-")
hold on
plot(fj,Pb208,"b-")
hold off

mdlDawson208=fitnlm(fj,Pb208,GaussFit,beta208);
beta208 = mdlDawson208.Coefficients.Estimate;
Errors208=mdlDawson208.Coefficients.SE;

[beta208,Errors208];

figure
plot(fj,GaussFit(beta208,fj),"r-",'LineWidth',3)
hold on
plot(fj,Pb208,"b.",'MarkerSize',20)
hold off
```

```

figure
plot(fj,mdlDawson208.Residuals.Raw,"bo-","LineWidth",2)
hold off
fprintf('\n Mean squared residuals for scan %d: %.4f\n', n, sum(mdlDawson208.Residuals.Raw.^2) / length(mdlDawson208.Residuals.Raw));



%TIS406=-0.5.*((beta208(2)-beta208(13))+(beta208(5)-beta208(11)));
%TIS939=0.5.*((beta208(2)-beta208(13))-(beta208(5)-beta208(11))).*(f939/f406);
%Uncertainty=(Errors208(2).^2+Errors208(13).^2+Errors208(5).^2+Errors208(11).^2).^0.5;

%TISS406(n)=1000.*TIS406;
%TISS939(n)=1000.*TIS939;
%Uncertainties(n)=1000.*Uncertainty;

%[beta208(3)',Errors208(3)',beta208(6)',Errors208(6)',beta208(8)',Errors208(8)',beta208(10)',Errors208(10)'];


%[fj',Pb208,GaussFit(beta208,fj)']
%Splitting=beta208(5)-beta208(2)
%UncertaintySplitting=(Errors208(2).^2+Errors208(5).^2)^(1/2)

IsotopeShift406206208=1000.*((beta208(3)-beta208(10))+(beta208(6)-beta208(8))).*0.5;
Error406206208=1000.*0.5.*sqrt(Errors208(3).^2+Errors208(8).^2+Errors208(6).^2+Errors208(10).^2+((UncFSR/FSR).*IsotopeShift406206208.*0.001).^2);

IsotopeShift939206208=1000.*((beta208(3)+beta208(10))-(beta208(6)+beta208(8))).*0.5.*(405.8./938.9);
Error939206208=sqrt((1000.*0.5.*(405.8./938.9).*sqrt(Errors208(3).^2+Errors208(8).^2+Errors208(6).^2+Errors208(10).^2)).^2+((UncFSR/FSR).*IsotopeShift939206208.*0.001).^2);

IsotopeShift406204208=1000.*((beta208(3)-beta208(17))+(beta208
```

```
(6)-beta208(15))).*0.5;
Error406204208=1000.*0.5.*sqrt(Errors208(3).^2+Errors208(17).^2+Errors208(6).^2+Errors208(15).^2+((UncFSR/FSR).*IsotopeShift406204208.*0.001).^2);

IsotopeShift939204208=1000.*((beta208(3)+beta208(17))-(beta208(6)+beta208(15))).*0.5.*(405.8./938.9);
Error939204208=sqrt((1000.*0.5.*(405.8./938.9).*sqrt(Errors208(3).^2+Errors208(17).^2+Errors208(6).^2+Errors208(15).^2)).^2+((UncFSR/FSR).*IsotopeShift939204208.*0.001).^2);


HFConstant=1000.*(beta208(6)-beta208(3))./2.5;
ErrorHFConstant=1000.*0.5.*sqrt(Errors208(3).^2+Errors208(6).^2)*(2/5);

UHFConstant=1000.*(beta208(10)-beta208(3))./1.5;
ErrorUHFConstant=1000.*0.5.*sqrt(Errors208(3).^2+Errors208(9).^2)*(2/3);

%IsotopeShift939=1000.*((beta208(3)-beta208(6))/(3/2));
%Error939=1000.*0.5.*sqrt(Errors208(3).^2+Errors208(6).^2)*(2/3);

fprintf('\n The Free Spectral Range is %.1f +/- %.1f MHz', 1000.*FSR,1000.*UncFSR)
fprintf('\n The 208-206 406 nm Transition Isotope Shift is %.1f +/- %.1f MHz', IsotopeShift406206208,Error406206208)
fprintf('\n The 208-206 939 nm Transition Isotope Shift is %.1f +/- %.1f MHz', IsotopeShift939206208,Error939206208)
fprintf('\n The 208-204 406 nm Transition Isotope Shift is %.1f +/- %.1f MHz', IsotopeShift406204208,Error406204208)
fprintf('\n The 208-204 939 nm Transition Isotope Shift is %.1f +/- %.1f MHz', IsotopeShift939204208,Error939204208)


%fprintf('\n The (6p^2) 3P2HF Constant is %.1f +/- %.1f MHz', HFConstant,ErrorHFConstant)
%fprintf('\n The (6p7s) 3P1 HF Constant is %.1f +/- %.1f MHz', UHFConstant,ErrorUHFConstant)


```

```

TIS406206208(n)=IsotopeShift406206208;
ETIS406206208(n)=Error406206208;
TIS939206208(n)=IsotopeShift939206208;
ETIS939206208(n)=Error939206208;
TIS406204208(n)=IsotopeShift406204208;
ETIS406204208(n)=Error406204208;
TIS939204208(n)=IsotopeShift939204208;
ETIS939204208(n)=Error939204208;
HFC(n)=HFConstant;
EHFC(n)=ErrorHFConstant;
UHFC(n)=UHFConstant;
EUHFC(n)=ErrorUHFConstant;
FreeSpectralRange(n)=FSR;
EFSR(n)=UncFSR;

end

%[TIS406206208', ETIS406206208']
%[TIS939206208',ETIS939206208']

[TIS406206208', ETIS406206208',TIS406204208', ETIS406204208']
[TIS939206208',ETIS939206208',TIS939204208',ETIS939204208']
%[FreeSpectralRange',EFSR']

%[HFC', EHFC']
%[UHFC', EUHFC']

Average406206208=mean(TIS406206208);
Error406206208mean=std(TIS406206208)./sqrt(NoScans);
Average939206208=mean(TIS939206208);
Error939206208mean=std(TIS939206208)./sqrt(NoScans);
Average406204208=mean(TIS406204208);
Error406204208mean=std(TIS406204208)./sqrt(NoScans);
Average939204208=mean(TIS939204208);
Error939204208mean=std(TIS939204208)./sqrt(NoScans);

AverageHFConstant=mean(HFC);
ErrorHFConstantmean=std(HFC)./sqrt(NoScans);

AverageUHFConstant=mean(UHFC);
ErrorUHFConstantmean=std(UHFC)./sqrt(NoScans);
```

```
fprintf('\n The OVERALL 206-208 406 nm TIS is %.1f +/- %.1f MHz',Average406206208,Error406206208mean)
fprintf('\n The OVERALL 206-208 939 nm TIS is %.1f +/- %.1f MHz', Average939206208,Error939206208mean)
fprintf('\n The OVERALL 204-208 406 nm TIS is %.1f +/- %.1f MHz',Average406204208,Error406204208mean)
fprintf('\n The OVERALL 204-208 939 nm TIS is %.1f +/- %.1f MHz', Average939204208,Error939204208mean)

%fprintf('\n The OVERALL (6p^2) 3P2 HF Constant is %.1f +/- %.1f MHz', AverageHFConstant,ErrorHFConstantmean)
%fprintf('\n The OVERALL (6p7s) 3P1 HF Constant is %.1f +/- %.1f MHz', AverageUHFConstant,ErrorUHFConstantmean)
```

Bibliography

[1] N. B. Vilas, B.-Y. Wang, P. M. Rupasinghe, D. L. Maser, M. S. Safronova, U. I. Safronova, and P. K. Majumder, Phys. Rev. A **97**, 022507 (2018), URL `https://link.aps.org/doi/10.1103/PhysRevA.97.022507`.

[2] D. L. Maser, E. Hoenig, B.-Y. Wang, P. M. Rupasinghe, S. G. Porsev, M. S. Safronova, and P. K. Majumder, Phys. Rev. A **100**, 052506 (2019), URL `https://link.aps.org/doi/10.1103/PhysRevA.100.052506`.

[3] S. G. Porsev, M. G. Kozlov, M. S. Safronova, and I. I. Tupitsyn, Phys. Rev. A **93**, 012501 (2016), URL `https://link.aps.org/doi/10.1103/PhysRevA.93.012501`.

[4] PubChem, *Atomic radius — periodic table of elements*, URL `https://pubchem.ncbi.nlm.nih.gov/ptable/atomic-radius/`.

[5] *Atomic Data for Lead (Pb) — physics.nist.gov*, `https://physics.nist.gov/PhysRefData/Handbook` [Accessed 17-04-2025].

[6] J. H. Lacy, A. C. Kinney, and P. K. Majumder, Phys. Rev. A **111**, 042808 (2025), URL `https://link.aps.org/doi/10.1103/PhysRevA.111.042808`.

[7] G. Ranjit, D. Kealhofer, G. D. Vukasin, and P. K. Majumder, Phys. Rev. A **89**, 012511 (2014), URL `https://link.aps.org/doi/10.1103/PhysRevA.89.012511`.

[8] S. Bouazza, D. S. Gough, P. Hannaford, R. M. Lowe, and M. Wilson, Phys. Rev. A **63**, 012516 (2000), URL `https://link.aps.org/doi/10.1103/PhysRevA.63.012516`.

[9] J. R. Persson, Journal of Physics Communications **2**, 055028 (2018), URL `https://dx.doi.org/10.1088/2399-6528/aac52b`.

[10] J. M. Reeves and E. N. Fortson, Phys. Rev. A **44**, R1439 (1991), URL `https://link.aps.org/doi/10.1103/PhysRevA.44.R1439`.

[11] D. J. Griffiths, *Introduction to Quantum Mechanics (2nd Edition)* (Pearson Prentice Hall, Upper Saddle River, NJ, 2004).

[12] C. J. Foot, *Atomic Physics* (Oxford University Press, 2005).

[13] G. K. Woodgate, *Elementary Atomic Structure* (Oxford University Press, 1983).

[14] H. Davis, *Fourier Series and Orthogonal Functions* (Dover Publications, 2012).

[15] C. Yang, Ph.D. thesis, Williams College (2024).

[16] A. Kinney, Ph.D. thesis, Williams College (2024).

[17] E. M. Purcell and G. B. Field, **124**, 542 (1956).